
Ni-Cu-Co-rich hydrothermal manganese mineralization in the Wallis and Futuna back-arc environment (SW Pacific)

Pelleter Ewan^{1,*}, Fouquet Yves¹, Etoubleau Joel¹, Cheron Sandrine¹, Labanieh Shasa¹,
Josso Pierre¹, Langlade Jessica²

¹ Ifremer, Unité de Recherche Géosciences Marines, F-29280 Plouzané, France

² CNRS, Ifremer c/Brest, F-29280 Plouzane, France

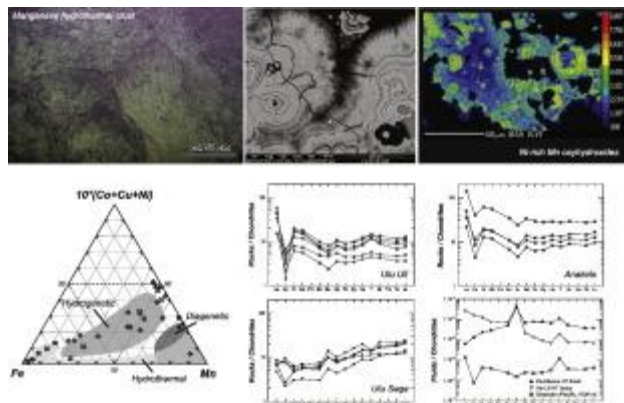
* Corresponding author : Ewan Pelleter, email address : ewan.pelleter@ifremer.fr

Abstract :

The Wallis and Futuna back-arc system is a complex area composed of at least two active oceanic spreading centers (Futuna and Alofi spreading centers) and young volcanic zones characterized by diffuse magmatism locally affected by the Samoan hotspot. This geological setting is favorable to the establishment of hydrothermal systems either high-temperature (HT) hydrothermal venting or low-temperature (LT) diffuse flow. During the 2010 Futuna cruise aboard R/V L'Atalante, three remarkable inactive LT Fe-Si-Mn deposits have been discovered (i.e. Utu Uli, Anakele and Utu Segá). Some of the Mn-rich precipitates exhibit the highest base metals concentrations so far recorded in ferromanganese rocks including the well-documented hydrogenetic crusts and polymetallic nodules. The deposits lie on top of the volcanoes and formed in close association with the volcanic facies. The manganese mineralization occurs as massive layered crust and Mn-rich cements within strongly altered basaltic pyroclastic rocks, brecciated lavas and rarely sediments. Field observations, mineralogical and chemical studies support a hydrothermal origin for the mineralization and show that nickel, cobalt and copper enrichments are controlled by the precipitation of 7 Å and 10 Å manganates. The conventional geochemical classifications (e.g. Bonatti et al., 1972) used to decipher the origin of Mn mineralization can no longer be used for this new type of deposit and new robust discrimination diagrams need to be established. We suggest that the unusual enrichment of metals recorded in our samples is due to: (i) lack of precipitation of high-temperature massive sulfides at depths which would have retained metals (e.g. Cu, Ni, Co); (ii) the isolation of the hydrothermal system avoiding Ni, Co and Cu losses in the water column; and (iii) the ability of birnessite and buserite/todorokite to strongly scavenge Co, Ni, and Cu from aqueous fluids. The Utu Uli and Anakele deposits share some common characters with the active hydrothermal system at Loihi seamount (e.g. depth of mineralization, relationship with pyroclastic volcanoes, and influence of a mantle plume source) and thus, might represent the late-stage products of this specific type of hydrothermal activity. Besides, the Co-rich mineralization of the Calatrava volcanic field (Spain) may be a potential analog of the Utu Segá deposit. The CVF Mn-(Co) deposits formed in close proximity to Pliocene volcanic rocks. In those deposits, metals were transported by epithermal hydrothermal solutions with high fO₂ and cobalt was strongly scavenged by Mn oxides. Together with the well-documented stratabound Mn deposits (González et al., 2016; Hein et al., 2008; Hein et al., 1996), the Mn deposits discovered in the Wallis and Futuna back-arc provide crucial insights for understanding the low temperature hydrothermal activity in the deep ocean. The metal-rich character of this low-temperature hydrothermal activity may be of major importance for future research on the net

flux of hydrothermally derived metals (e.g. Ni, Co, Cu) to the open ocean.

Graphical abstract



Highlights

- ▶ We found atypical Ni-, Co-, Cu-rich Mn-Fe-Si precipitates in the Wallis and Futuna back arc system
- ▶ Field observations, mineralogical and geochemical studies highlight a hydrothermal origin for the mineralization
- ▶ Large trace metals variations among samples might be due to the evolution of the physical and chemical factors of the hydrothermal fluids
- ▶ The Utu Uli and Anakele deposits share some common characters with the active hydrothermal system at Loihi seamount
- ▶ The Utu Sega appears similar to the stratabound Mn deposits and the Co-rich Mn deposits of the Calatrava Volcanic Field (Spain)

Keywords : Hydrothermal, Diffuse flow, Manganese oxyhydroxides, Metal-rich, Seafloor, Wallis and Futuna Island, South-West Pacific

1- Introduction

Ferromanganese mineralization occur in nearly all deep-sea environments and are formed by three main processes (Hein et al., 1997): (i) precipitation of iron and manganese oxyhydroxides colloids from cold ambient seawater, (ii) precipitation from pore waters and (iii) precipitation from hydrothermal fluids. The first two processes lead to the formation of ferromanganese crusts and polymetallic nodules respectively whereas the third mechanism is related to the formation of Fe-Mn±Si deposits. With a narrow range of Fe/Mn ratio (ca. 1) and high concentrations of Co, Ni, Cu, REE (Rare Earth Elements), HFSE (High Field Strength Elements), Te and Pt, ferromanganese crusts are presently regarded as a potential mineral resource (Hein et al., 2013). Polymetallic nodules exhibit a wide range of Fe/Mn ratio (1 to 15) and metals contents (Cronan, 1997; Dymond et al., 1984) and may be of economic interest for Cu and Ni in specific environments (e.g. Clarion and Clipperton fractures zone). Ferromanganese deposits precipitated from hydrothermal processes show a broad range of compositions going from pure Mn oxides to almost pure Fe oxides with the highly variable amount of amorphous silica and/or nontronite. They usually exhibit low to very low metals contents owing to sulfides fractionation at depths (e.g. Glasby et al., 1997; Hein et al., 2008), minor metals leaching of igneous rocks by low temperature hydrothermal fluids and/or discharge of metals to the water column before Mn oxyhydroxides precipitation. However, several stratabound hydrothermal Mn deposits located in back-arc basins (e.g. Fouquet et al., 1993; Kuhn et al., 2003), active hot spot volcanoes (Hein et al., 1996, 1992), arc system (Hein et al., 2008, 1990) and margin setting (González et al., 2016) display slightly anomalous trace elements contents (e.g. Mo, Ni, Cd, Zn, Cd, Cu, Co). These deposits are generally interpreted as the distal precipitates of high-temperature systems that produce massive sulfides and sulfates (Hein et al., 2008; Kuhn et al. 2003).

In 2010, exploration of the French exclusive economic zone of Wallis and Futuna during the Futuna cruise aboard R/V L'Atalante led to the discovery of three remarkable hydrothermal ferromanganese deposits (Utu Uli, Anakele and Utu Segá; Fig. 1). This paper describes the sampled Fe-Si-Mn precipitates some of which exhibiting the highest base metals concentrations so far recorded in ferromanganese rocks including the well-documented hydrogenetic crusts and polymetallic nodules (Hein et al., 2015, 1997). The objective of this study is to document these atypical Fe-Si-Mn precipitates that question the classical view of low temperature hydrothermal activity in the deep ocean.

2- Geological Setting and Sampling Sites

The Wallis, Futuna and Alofi islands are located in a key area of the Pacific-Australia plate boundary. They are bordered by the North Fiji fracture zone, the active Tonga-Kermadec subduction zone and

the related Lau and North Fiji back-arc basins and, the currently active Samoan plume. This situation between the northern end of the Tonga trench and the regional Fiji transform fault account for the complex volcanic and tectonic activity in the area. Previous investigations had revealed multiple active extensional zones including well organized spreading centers such as the FUTUNA and ALOFI oceanic ridge (Fouquet et al., 2015; Pelletier et al., 2001)(Fig. 1) and several areas of numerous and diffuse magmatic centers (e.g. Southeast Futuna volcanic zone ; Pelletier et al., 2001). West of the Futuna Island, the 20-30° trending Futuna spreading center is composed of a series of en echelon spreading segments. The opening rate of this oceanic ridge has been estimated at 4cm/yr from the interpretation of magnetic anomalies (Pelletier et al., 2001). South-east of the Futuna Island, bathymetric maps and reflectivity data clearly reveals that active extension and recent volcanism occurs in the Southeast Futuna volcanic zone and along the Alofi spreading center (Fouquet et al., 2015; Pelletier et al., 2001).

Geochemical compositions of the lavas collected during the FUTUNA cruise are related to partial melting of an Indian-like mantle that has been significantly metasomatized by an enriched end-member composed of the Samoan plume material (Labanieh et al., 2011). The influence of the Samoan plume is stronger west of the Futuna Island particularly in the northern part of the Futuna spreading center.

The Utu Uli deposit is located at the northern tip of the Futuna oceanic ridge axis. Two manned submersible dives and two dredge operations have been done successfully. The deposit is controlled by a line of several small sub-circular volcanoes (Fig. 2A). These volcanic edifices are mainly composed of pyroclastic rocks and highly vesicular basaltic pillows lavas exhibiting a trace elements chemical composition similar to the Oceanic Island Basalt of the Samoan hotplume (Labanieh et al., 2011). The manganese mineralization (Fig. 3A, B, and C) range from 800 m to 1,000 meter below sea level (mbsl) and cover at least three distinct volcanic edifices for a total surface area of approximately 1.5 km² (ca. 1.5km x 1 km). The manganese mineralization lying on the flanks of the volcanoes consist of layered Mn crusts up to 5 cm in thickness. The bathymetric highs exhibit both layered crust with bread-crust like fractures (Fig. 3A) and decimetric-to-metric mounds. Locally, the manganese crust is crosscut by iron and silica-rich crest and/or vein, up to 1m high, which likely reflect pulses of hydrothermal activity (Fig. 3 B, C).

The Anakele deposit is located on a broad (ca. 5km x 5km) individual pancake-like volcano, 20 km east of the southern part of the Futuna ridge. It was studied during one manned submersible dive and additional sampling was performed during a dredge operation (Fig. 2B). The manganese mineralization (Fig. 3D, E, and F) has been observed at the top of the volcanic edifice. The magmatic rocks are composed of pyroclastic rocks and basaltic pillows lavas locally covered by a thick sedimentary cover and rarely by 1-cm-thick hydrogenetic Fe-Mn crust. The two topographic highs

near the top (> 1600 mbsl) might represent small individual pyroclastic volcanoes and are systematically covered by manganese mineralization. Due to high sediment accumulations in the depressions, the continuity of the mineralization remains unclear. However, the mineralized area which ranges from 1,750 to 1,560 mbsl might be as widespread as the Utu'Uli mineralization (ca. 1.5km²). The manganese oxyhydroxides form layered smooth to granular Mn crusts crosscut by Fe-Si-rich precipitates. The yellow, reddish yellow and red color observed right beneath the crusts (Fig. 3D, E) is related to the high proportion of iron oxyhydroxides with a minor amount of yellow nontronite. The Utu Sega deposit was sampled by dredging on a NNE-SSW trending ridge located 5 km west of the Alofi oceanic ridge axis (Fig. 1 and Fig. 2). Dredged volcanic rocks include strongly altered basaltic pillow lavas and volcanic breccias. The mineralization is dominated by dense and laminated manganese precipitates.

While the hydrothermal character of the mineralization is expected from in-situ observations, there is, to date, no evidence of a current hydrothermal discharge in the close vicinity of the three deposits.

3- Samples and Methods

Samples were collected during cruise FUTUNA aboard the R/V L'Atalante in 2010. This cruise was dedicated to regional mapping and the exploration for polymetallic sulfides of the French Exclusive Economic Zone (EEZ) around the Wallis and Futuna Islands. Dredge hauls and dives (HOV Nautilie) were performed to sample the mineralization. Selected samples were labeled according to the name of the cruise (FU for FUTUNA), the type of sampling tool (DR for dredge hauls; PL for diving operations), the number of the operation and a rock designation number (e.g. FU-DR15-01). Samples were characterized and prepared directly on-board. Rocks were cut and dried in an air oven at 50°C. A representative portion of each sample was ground to a fine powder using an agate mortar.

Mineralogical and quantitative chemical data were acquired using X-ray techniques (X-ray diffraction and X-ray fluorescence) at the Laboratoire de Géochimie et Métallogénie at IFREMER institute (Brest, France).

X-ray diffraction (XRD) analyses were conducted with a BRUKER AXS D8 Advance and a BRUKER D2 PHASER diffractometer. Samples were top loaded into 2.5 cm diameter circular cavity holders, and all analyses were run between 5° and 70°2θ, with 0.01°2θ step at 1s/step (monochromatic Cu Kα radiation, 40 kV, 30mA). Minerals were identified using Diffrac.Suite EVA software. This methodology allows to quickly identifying most of the minerals enclosed in our samples (e.g. silicates, carbonates, well-crystallized manganates, well-crystallized oxyhydroxides). For manganates characterization, the analysis was performed directly on board and two month later in the laboratory. Additionally, a new

run on selected samples was done five years later to evaluate the possible collapse of 10 Å magnanates to 7 Å manganates with time.

For clays characterization, a separated fraction ($< 2\mu\text{m}$) was investigated on two types of oriented mounts (air-dried and glycol-saturated) from 2 to $40^\circ 2\theta$, step of $0.01^\circ 2\theta$, at 1s/step (monochromatic Cu $K\alpha$ radiation, 40 kV, 30mA). A randomly oriented sample was prepared to identify trio- or dioctahedral clay minerals (e.g. nontronite) from the 060 reflections (57 to $64^\circ 2\theta$, step of $0.02^\circ 2\theta$, at 120s/step).

X-ray fluorescence analyses were conducted with a wavelength dispersive X-ray fluorescence spectrometer (WD-XRF; BRUKER AXS S8 TIGER) on fusion beads or compressed pellets (for major and trace elements, respectively). After data acquisition, measured net peak intensities corrected from inter-element effects were converted into concentrations using calibration curves generated from the analysis of certified geochemical standard powders, measured under identical analytical conditions.

Scanning electron microscopy (SEM) investigations were done with a FEI Quanta 200 SEM on C-coated polished sections and small fragments ($1\text{mm} \times 1\text{mm}$) of manganese mineralization. Secondary electron and backscattered images were performed for textural characterization of the Mn oxides.

Mineral analyses were performed on C-coated polished sections with a Cameca SX100 electron microprobe (Microsonde Ouest, Brest, France) operating in the wavelength dispersive mode. Operating conditions for spot analyses were set to 15 keV, 20 nA and 10 s counting time on the peak (spot size = $1\mu\text{m}$). The $\phi(\rho Z)$ matrix correction was applied based on Pouchou and Pichoir (1988). Standards (element, emission line) are: albite (Na $K\alpha$, Si $K\alpha$), InP (P $K\alpha$), forsterite (Mg $K\alpha$), corundum (Al $K\alpha$), orthose (K $K\alpha$), wollastonite (Ca $K\alpha$), synthetic manganese titanate (Mn $K\alpha$, Ti $K\alpha$), pure iron (Fe $K\alpha$), pure cobalt (Co $K\alpha$), pure nickel (Ni $K\alpha$), pure copper (Cu $K\alpha$), sphalerite (Zn $K\alpha$), pure molybdenum (Mo $K\alpha$), barytine (Ba $K\alpha$). X-ray quantitative element maps have been elaborated with the software SX100. The same analytical setup used for point analyses was also used for mapping, so that a common set of calibration intensities was used for quantification of both point and map data. Electron microprobe spot analyses and chemical maps were performed to evaluate both the differences among Mn oxides precipitated in contact with seawater (i.e. layered massive microcrystalline crust) or developed at subsurface and the differences among the crystallites (C), microcrystallites (MC) and amorphous cryptocrystallines (AC) Mn oxides.

Pearson coefficient correlation matrix was calculated on the i) whole data set ($n=35$), ii) volcanic- and/or sediment-free mineralized samples ($n=21$), iii) Utu Uli volcanic- and/or sediment-free mineralized samples ($n=14$) and iv) Anakele mineralized samples ($n=10$) (Supplementary Table S1, S2, S3 and S4). Si, Al, Fe, Mn, Ca, Mg, K, Na, Ti, P, V, Co, Ni, Cu, Zn, As, Sr, Y, Ba, Mo were taken into account in order to extract information on possible phase and/or element associations. The zero

correlations were calculated at the 95% confidence and statistically significant correlations were underlined.

4- Results

4.1- Sample Morphology and Mineralogy

Overall, we studied 35 mineralized samples (Utu Uli: n=20; Anakele: n=10; Utu Sega: n=5) which encompass a wide range of mineralogical and geochemical types from pure Mn oxide to nearly pure Fe-Si rocks with variable amount of altered pyroclastic rocks and minor sediments.

At Utu'Uli and Anakele, the mineralization formed directly onto the seafloor and includes black manganese crust (up to 2-cm-thick) composed of dense and massive Mn oxyhydroxides with a metallic gray luster (Fig. 4A) and Fe-Si crests composed of X-ray amorphous iron oxyhydroxides and opal (Fig. 4B). The mineralization right beneath the layered crust display breccia-like texture resulting from cementation by Mn oxyhydroxides of highly vesicular lapilli, volcanic bombs and glass shards (Fig. 4C, D). The pyroclastic material is strongly altered and pristine mineralogy is commonly fully replaced by nontronite and/or iron and manganese oxyhydroxides (Fig. 4C). One sample (FU-DR-01-03; Fig. 4A) provides an outstanding section of the first centimeter of the mineralization with the 2-cm-thick massive and laminated crust overlying the fully altered, Mn-cemented pyroclastic rocks. Besides, several samples display a striking mineralogical zoning which, from top to bottom, is composed of Mn oxides, Fe oxides and yellow to green nontronite (Fig. 4D). The thickness of the manganese layer is variable but can reach 10cm in few samples.

At Utu Sega, the five mineralized samples are mainly composed of Mn oxides that occur as pale gray to dark gray stratiform layers with submetallic to metallic luster (Fig. 4F). Three rocks (FU-DR-22-02, FU-DR-22-04 and FU-DR-22-06) consist of alternating thin foraminiferous-rich beds and Mn oxide laminae with no or rare iron oxides. One mineralized rock (FU-DR-22-03) is also characterized by infilling of fractures by Mn oxides in strongly altered volcanic breccias. The manganese-rich samples collected at Utu Sega resembles the stratabound Mn described by Hein et al. (2008) along the Mariana and Izu-Bonin arc system.

4.1.1- Mn oxide mineralogy and texture

XRD studies show that Mn oxides consist mostly of a mixture of well-crystallized 7 Å (birnessite) and 10 Å (todorokite and/or "buserite") manganates. Vernadite (δ -MnO₂) might be present but the two X-ray diffraction reflections at ca. 2.46 Å and 1.42 Å are overlapped by the XRD reflections of the birnessite and/or todorokite/"buserite". This explains why the vernadite is difficult to identify when accompanied by large proportion of 7 Å and/or 10 Å manganates. Distinction between todorokite

and “buserite” is not possible with X-ray analyses alone since these two 10 Å manganates have similar X-ray diffraction reflections (Burns and Burns, 1977). The 10 Å interlayer spacing of “buserite” is known to collapse to the typical 7 Å birnessite spacing upon drying. In our samples, we cannot exclude a rapid collapse of the “buserite” upon drying before the first XRD analysis at sea (ca. 12h after sampling). After three month, 10 Å manganates were clearly visible in more than half of the mineralized rocks. After five years, the transformation has progressed but 10 Å manganate was still detected in todrokitite and/or “buserite”-rich samples. These observations support that two types of 10 Å manganates might exist in our samples: one is a mineral that collapse to 7 Å manganate through time and the other is a manganate that does not collapse after drying.

As a consequence, we must consider with caution the relative proportions of well-crystallized 7 Å and 10 Å manganates in our samples which reflect the qualitative assessment of diffractograms acquired three months after sampling.

Mn oxides found in Utu Uli samples include significant proportion of 10 Å manganates (up to 65% of the manganates). The uppermost layered crust that crops out at the seafloor-seawater interface displays the highest amount of 10 Å manganates whereas the subsurface Mn oxides with breccia-like texture are dominated by birnessite. Mn oxides found in Anakele samples are predominantly composed of 7 Å birnessite (89 – 100 %) and the Mn samples collected at Utu Sega show a high proportion of 10 Å manganates (36 – 82 %) still present 5 years after sampling with no significant collapse to 7 Å Mn oxides.

From the study of polished sections and fragments of selected samples, two types of textures were distinguished: (i) the massive and dense microcrystalline Mn oxides related to the precipitation of crust at the seafloor-seawater interface, (ii) the crystallization of Mn oxides in interstices of unconsolidated host rocks or, more rarely, fractures in volcanic breccias.

The first textural type (Fig. 5A) is characterized by homogeneous and laminated dense layers composed of microcrystalline Mn oxides. The manganates grew on unconsolidated pyroclastic rocks and are composed of botryoids that coalesce into layers densely packed and with low pore space between them. SEM images of small crust fragments (Fig. 6A) show a low porosity and a homogeneous crystallinity portrayed by the presence of small-sized Mn oxides ($\leq 1 \mu\text{m}$).

The Mn oxides in the interstices have a radial fibrous to spherulitic texture (Fig. 5B, C, D, E) that may coalesces to form scallop-like (Fig. 5F) and/or columnar (Fig. 6B) morphologies. Within those textures, three mineral-size classes can be described: (i) amorphous cryptocrystalline oxides (AC), (ii) microcrystalline oxides (M) and (iii) crystalline oxides (C) (Fig. 6B, C, E). These classes are similar to those described by Hein et al. (2008) in stratabound Mn deposits from the Mariana and Izu-Bonin volcanic arcs. Individual spherules and radial fibrous structures are composed of alternating laminae of microcrystallites and crystallites and generally display an amorphous cryptocrystalline core (Fig.

5C, D and Fig. 6D). In stratabound Mn deposits (Hein et al., 2008), this alternation of AC, M and C oxides was interpreted as an evidence of the waxing and waning stages of the hydrothermal fluid and mixing with oxygenated pore fluids. Amorphous cryptocrystalline Mn oxides reflect a rapid precipitation (waxing stage) and the microcrystallites and crystallites (up to 600 μm in size at Anakele; Fig. 5E and Fig. 6E, F) suggest a slower precipitation.

4.2- Sample Geochemistry and Growth Rates

4.2.1- Bulk-rock composition

The chemical compositions of the Fe-Si-Mn mineralization are given in Table 1. Samples display a wide range of Fe/Mn ratio from nearly pure manganese oxides (e.g. FU-DR01-06: Mn = 52 wt.%; Fe < 0.7 wt.% ;) to Fe-Si-rich rocks with very low amount of Mn (e.g. FU-PL08-04: Mn < 0.8 wt.%; Fe = 37.1 wt.%; Si = 10.3 wt.%). The strong fractionation of iron and manganese is diagnostic of hydrothermal precipitates and is related to the different solubilities of iron and manganese oxides in hydrothermal fluids (Krauskopf, 1957). Aluminium content is very low except for three samples which enclose significant proportion of volcanogenic clasts (FU-PL08-02, FU-PL08-06 and FU-DR22-03). Alumina is strongly correlated with titanium (correlation coefficient: 0.983; supplementary table S1) and, to a lesser extent, with magnesium (0.743; supplementary table S1) and calcium (0.624; supplementary table S1) reflecting the association of these elements in the aluminosilicate component (e.g. pyroclastic rocks). However, the relatively high calcium concentrations in the mineralization of Utu Segá are due to the presence of calcite. Except samples with high aluminosilicate and/or carbonate components, most samples can be modeled using a three-component system with Mn oxyhydroxide, Fe oxyhydroxide and nontronite (Fig. 7). The strong anti-correlation between, on one hand, Mn and, on the other hand, Fe (-0.938; supplementary table S1) and Si (-0.907; supplementary table S1) as well as the good correlation between Fe and Si (0.751; supplementary table S1) reflects the striking mineralogical zoning (i.e. Mn oxides, Fe oxides and nontronite) that characterizes the studied deposits. Sodium is strongly adsorbed to the surface of Mn oxides (Na and Mn: 0.843; supplementary table S1) whereas phosphates is scavenged by Fe oxides (P and Fe: 0.821; supplementary table S1).

Metals such as Ni, Cu, Co and Mo are unexpectedly enriched for Fe-Si-Mn mineralization that precipitated from a hydrothermal process. Nickel, cobalt, copper and molybdenum in manganese-rich samples (i.e. > 35 wt.% Mn) ranges respectively from 0.13 to 4.67 wt.%, 0.01 to 2.24 wt.%, 41 ppm to 1.53 wt.% and 0.05 to 0.18 wt.%. In details, there are strong differences in Ni, Co and Cu enrichment between the three deposits (Fig. 8A): Mn oxides are usually enriched with nickel at Utu Uli (Mn-Ni correlation: 0.777; supplementary table S3), copper at Anakele (Mn-Ni correlation: 0.905; supplementary table S4) and cobalt at Utu Segá. The highest metal concentrations are recorded in

the purest Mn oxide samples (Fig. 8B, C, D, E, F). The only exception is for samples with mineralogical and textural characteristics of Mn precipitates formed in contact with seawater (i.e. layered crust and Fe-Si±Mn crusts; e.g. FU-DR01-03, FU-PL10-08 and FU-DR15-11). The positive correlation observed between metals and Mn (Fig. 8B; supplementary table S2) is consistent with adsorption of metals by Mn oxyhydroxides (Post, 1999).

Barium is also high in some Mn oxide samples (up to 1296 ppm) but displays lower mean concentrations compared to Mn-stratabound mineralization analyzed by Hein et al. (2008, 1996) and González et al. (2016).

Total rare earth elements (REE) are low (12 – 121 ppm) consistent with the hydrothermal signature; if one outlier is not considered (FU-DR15-06; Anakele), the range of REE would be 12 to 41 ppm. Chondrites-normalized patterns (Sun and McDonough, 1989) of Utu Uli and Anakele samples are similar to the pattern for seawater (Fig. 9A, B) with light REE enrichment and a negative Ce anomaly (Ce/Ce^* : 0.04 – 0.49). At Utu Sega, Mn precipitates show a distinctive signature with low light REE concentrations (Fig. 9C), negative to positive Ce anomaly (Ce/Ce^* : 0.47 – 1.47) and a positive Eu anomaly (Eu/Eu^* : 1.18 – 1.72). In deep-sea environment, the positive europium anomaly is diagnostic of reduced, chlorine-rich hydrothermal fluids (e.g. Craddock et al., 2010; Douville et al., 1999; Michard, 1989; Michard and Albarède, 1986).

4.2.2- Classification of the mineralization

On the basis of the $(Co+Ni+Cu) \times 10$ -Fe-Mn ternary diagram (Bonatti et al., 1972; Toth, 1980), most of the Wallis and Futuna back-arc samples fall within two fields: (i) the hydrothermal and (ii) the hydrogenetic field (Fig. 10). The iron-silica rich samples plot in the hydrothermal field whereas samples with significant amount of Mn oxides fall within the hydrogenetic field. However, the purest Mn oxides samples of Utu Uli and Anakele plot outside of the three fields defined by Bonatti et al. (1972) owing to the unusually high metals concentrations. One exception is sample FU-DR01-03 which is classified as hydrothermal in the ternary diagram. This sample has a large proportion of the massive and laminated crust that precipitates directly on the seafloor. The Mn oxides samples of Utu Sega can be distinguished from others since they fall within the upper limit or outside the diagenetic field. In order to discriminate Mn oxides, other discrimination diagrams have been tested (Supplementary Fig. S1; Bau et al., 2014; Choi and Hariya, 1992; Dymond et al., 1984; Nicholson, 1992; Toth, 1980). They generally fall within two or three fields (i.e. hydrothermal, hydrogenetic, diagenetic) and sometimes outside defined fields. Basically, diagrams based on REE favor a hydrothermal origin whereas the diagrams based on transition metals point to a diagenetic or hydrogenetic origin. As proposed in previous study using discrimination diagrams based on transition metals (e.g. Conly et al., 2011; González et al., 2016; Hein et al., 2008), the samples that fall

outside the hydrothermal field must not be considered definitively as “not hydrothermal”. Instead, this should be viewed as the result of the extreme enrichment of Ni, Co and Cu.

4.2.3- Growth rates estimations

Owing to the extreme enrichment of cobalt in most of the precipitates studied here, the growth rates were not determined using the empirical equation of Manheim and Lanebostwick (1988) based on normalized Co concentrations. Its use would lead to growth rates as low as 0.16 mm/Ma which is unlikely even for hydrogenetic crust. An explanation could be that the abnormal growth rates reflect a large contribution of hydrothermally-derived cobalt. Since REE are expected to be low in deep-sea hydrothermal fluids (Douville et al., 2002) and that hydrothermal REE contribution can be traced by the presence of Eu positive anomaly, an alternative to the Co-flux model would be the use of the Ce_{xs} model (Kuhn et al., 1998). The Ce_{xs} is a parameter that quantifies the degree of decoupling of Ce from other REE and which is related to the growth rate. Following the empirical equation of Kuhn et al. (1998), growth rate ($mm.Ma^{-1}$) is:

$$GR = \frac{1.94 * 10^4}{Ce_{xs}^{1.43}}$$

$$\text{Where } Ce_{xs} = Ce_{Fe-Mn crust} - \left[\frac{Ce_{sw} Pr_{Fe-Mn crust}}{Pr_{sw}} \right]$$

$Ce_{Fe-Mn crust}$: Ce concentrations in the Fe-Mn crust; Ce_{sw} : Ce concentrations in seawater; Pr_{sw} and $Pr_{Fe-Mn crust}$: same as for Ce

Using this method, on the average, the Mn oxide samples of Utu Uli have the highest growth rates with four samples yielding rates over 9,000 mm/Ma. One sample is characterized by very high growth rate over 500,000 mm/Ma and two samples have rates of <4,500 mm/Ma. At Anakele, growth rates of manganese samples range from 240 to 6,716 mm/Ma. Only one sample, (FU-DR10-06; Table 3) yields a low rate of 240 mm/Ma. Since this sample is characterized by the highest total REE concentrations, the low growth rate could indicate a slight hydrogenetic component. The Mn oxide samples of Utu Sega have a growth rate that ranges from 1,719 to 144,408 mm/Ma. These might represent minimum growth rates for the Utu Sega sample since the presence of a positive Eu anomaly in REE patterns indicates a hydrothermally-derived REE contribution. Moreover, the REE contribution from volcanic components (FU-DR22-03; Al = 2.62 wt.%) may explain the lowest estimation of the growth rate (i.e. 1,719 mm/Ma). Overall, the estimated growth rates are fairly typical of hydrothermal Mn oxides (Hein et al., 2008). The maximum thickness of the manganese mineralization (ca. 10 cm) divided by the mean growth rates yields duration of precipitation of ca. 1,000-30,000 years. This estimation, however, doesn't take into account possible dissolution-precipitation processes that might have occurred during successive hydrothermal episodes.

4.2.4- Electron microprobe composition of manganese oxyhydroxides

Overall, the Mn oxides have high Mn contents (> 30 wt.%) and low Fe (< 2 wt.%) (Table 3). The relatively high amount of manganese, particularly in AC oxides, points to a small proportion of adsorbed water and a low porosity of the Mn oxides. The massive layered crust that precipitates onto seafloor has lower Mg and higher Na than the underneath Mn oxide cement. High sodium is typical of seafloor or near seafloor deposition and low magnesium might be indicative of its removal in clay minerals (e.g. nontronite) from the hydrothermal fluid during the alteration of basaltic rocks (Hein et al., 2008).

Chemical maps show that Ni, Co and Cu concentrations are systematically very low in the layered massive crust (Fig 11A) whereas these metals are high (several percent) in Mn oxides cement (Fig. 11B, C; Table 3). In Fig. 11B, the highest nickel concentrations seems confined close to the nontronite clasts; however the effect of either high porosity or epoxy resin dilution on the relative Ni depletion observed locally cannot be ruled out. Nevertheless, the replacement of nontronite clasts can be assumed both with the progressive depletion of Fe and Si and the increasing of Mn and Ni in nontronite. Residual signature of nontronite might also be suspected in Mn oxides from the relatively high Fe and Si concentrations recorded in manganates at the Mn oxides-clays transition zone.

EMP spot analyses and chemical maps show that, in general, Mn, Na and K increase with increasing crystallinity (Table 3). At the opposite, Fe, Si, Mg, Al and Ca decrease with increasing of crystallinity. AC Mn oxides have higher mean concentrations of Co than MC and C Mn oxides (Table 3). High contents of nickel and copper have been recorded in the three mineral-size classes; however AC oxides are lower in nickel than the microcrystallites (MC). It is clear from the observation of EMP chemical maps (Fig. 11C) that, cobalt, nickel and copper are decoupled. But cobalt is obviously not restricted to the AC core and is sometimes higher in crystallites (Fig. 11C). Areas, where Co is enriched, correspond to areas where nickel is systematically depleted and vice versa. Apparently, copper mostly follows nickel though its behavior is somewhat transitional between Co and Ni.

5- Discussion

5.1- Origin of Fe-Si-Mn precipitates of the Wallis and Futuna back-arc system

The Utu Uli deposit is probably the youngest deposit owing to its location at the axis of the northern edge of the Futuna spreading center. At Anakele, the volcanic edifice is located ca. 20km east of the Futuna spreading center. According to a spreading rate of 4cm/yr (Pelletier et al., 2001), the age of the volcanic rocks might be as young as 500,000 yrs. However, the presence of a 1-cm-thick

hydrogenetic crust (Fouquet et al., unpublished data, 2010) indicates that the main volcanic edifice could be significantly older (few Ma). An estimation of the age of the Mn oxides collected at Utu Segá is difficult as we have only little information on the local geology (no submersible dive). According to its location 20km west of the axis of the Alofi spreading center and considering a similar spreading rate than the Futuna ridge, the maximum age should be less than 1 Ma.

In-situ observations of ridges and crests at the surface of the deposit, the increasing of thickness of the mineralization towards the top, as well as mineralogical and textural evidence indicate that the Fe-Si-Mn precipitates formed from hydrothermal fluids circulating through a volcanic basement. The high content of either Fe or Mn and the large Fe/Mn fractionation also support a hydrothermal origin for the deposits. The pure iron-silica samples exhibit low metal contents (Fig. 8) as expected for hydrothermal precipitates. Conversely, concentrations of nickel, cobalt and copper in mixed iron-silica-manganese samples are comparable to those reported for hydrogenetic crusts (Fig. 8, Table 4). Besides, several Mn-rich samples exhibit Ni + Cu + Co contents that exceed 4.9 wt.% (Table 1) which represents, to the best knowledge of the authors, the highest base metals concentrations ever recorded for a bulk sample of deep-sea ferromanganese rock. However, the Mn oxide could not have formed by hydrogenetic or diagenetic processes because the time required to develop the precipitates is much longer (10cm: >10Ma; (Hein et al., 2000) than the estimated age of the deposits (see above discussion). Total REE concentrations, estimated growth rates, and chondrites-normalized REE patterns definitively ruled out a major classical hydrogenetic or diagenetic influence for the three deposits.

Several authors (e.g. Conly et al., 2011; González et al., 2016; Hein et al., 2008, 1996, 1992, 1990) previously suggest using the metal enrichment with caution when trying to decipher the formation processes of Fe-Mn mineralization. It is clear that the extreme and generalized enrichments of Co, Cu and Ni, we report for our hydrothermal Mn±Fe±Si precipitates could give misleading information on the origin of the mineralization (i.e. hydrogenetic, diagenetic, hydrothermal). This is particularly true when using the classical conventional discrimination diagrams mostly based on transition metals concentrations (Bonatti et al., 1972; Choi and Hariya, 1992; Nicholson, 1992; Toth, 1980).

Our samples exhibit low concentrations of so-called immobile elements (e.g. Ti, Zr, Y, REE) which are expected to be low in acidic, chlorine-rich hydrothermal fluids (Douville et al., 2002). Thus, the best way to discriminate metals-rich hydrothermal Mn oxides is to use some of these trace elements as proposed by Bau et al. (2014) and Josso et al. (this volume)

5.2 Source(s) of the metals

Obviously, the metals enrichment reported in our samples (Ni, Co, Cu) make the Utu Uli, Anakele and Utu Segá deposits rather unusual. Relative high contents of trace metals were documented for

stratabound hydrothermal Mn deposits in different tectonic settings (e.g. González et al., 2016; Hein et al., 2008, 1996; Kuhn et al., 2003) though the Ni, Co, and Cu concentrations are commonly more than one order of magnitude lower than those of the deposits studied here (Table 4). Authors proposed different source components to explain the large chemical variations of trace elements such as Mo, Ni, Cr, Cu, Zn, Co, Pb or Ba. For example, the leaching of ultramafic rocks is assumed for the high Ni (up to 0.58 wt.%) and Cr (up to 0.15 wt.%) of the stratabound Mn samples from the Yap arc (Hein et al., 1992). Other sources include leaching of igneous rocks of different compositions, sulfides mineralization, biogenic sediments and/or the addition of metals from seawater (e.g. González et al., 2016; Hein et al., 2008, 1996, 1990; Kuhn et al., 2003; Moorby et al., 1984; Rogers et al., 2001). From the above discussion (see 5.1), a major seawater contributions for Ni, Co and Cu can be ruled out either because of the geological setting, the textural and mineralogical features, the fast precipitation of Mn oxides and the lack of correlations between these metals and the elements commonly enriched by a hydrogenetic process (e.g. REE, Ti, Zr). The Ni-rich Mn oxides analyzed with the electron microprobe systematically have chromium concentrations below the detection limit (i.e. <500 ppm). The absence of chromium anomalies even for Mn oxides with up to 5 wt.% Ni seemingly precludes an ultramafic origin for nickel (Hein et al., 2008). In addition, except in a deep fault Est of the Alofi island, no exposure of ultramafic rocks are identified in the Futuna area. A remobilization of massive sulfide bodies by the hydrothermal fluids that precipitated the Mn oxides is also unlikely owing to the low Zn, Cd and Pb concentrations (Table 4) and the fact that Cu and Co does not correlate with Zn in Mn oxides samples. In addition, typical sulfide deposits associated with basaltic rocks are not enriched in Ni (Fouquet et al., 2010). The mean average concentrations of calcium and barium of Utu Uli and Anakele is lower than those reported for the Valu Fa ridge, the Mariana, Izu bonin, Tonga and Yap arc and the Hawaii rift zone (Table 4) (Hein et al., 1997). High calcium contents in Utu Sega Mn oxide samples are rather related to the presence of calcite than to significant Ca enrichment in Mn oxides. Electron microprobe analyses confirm the relatively low calcium concentration in Mn oxides (Table 3). As a consequence, biogenic sediments may not have contributed significantly to the Ni, Cu- and Co-rich composition of the Mn oxides. Relatively low Ba and Sr concentrations support the low influence of sediments, although it also might also reflect the precipitation of barite at depth.

Collectively, these lines of evidence favor a volcanic source for Ni, Co and Cu rather than a product of the leaching of massive sulfides, ultramafic rocks or biogenic sediments.

Molybdenum contents are similar to other Mo-rich hydrothermal Mn precipitates (e.g. Hein et al., 2008, 1990; Krasnov et al., 1995; Kuhn et al., 2003; Moorby et al., 1984; T. D. S. Rogers, 2001). Enrichment of molybdenum in deep-sea Mn mineralization can originates from the intense leaching of volcanic rocks (Hein et al., 2008; Kuhn et al., 2003), high temperature sulfides (Hein et al., 2008;

Krasnov et al., 1995) and/or direct adsorption from seawater (Goto et al., 2015). The fact that neither Cu nor Zn correlates with Mo indicates that sulfides were not the predominant source for Mo in our samples. Hein et al (2008) suggest that the molybdenum enrichment recorded in the stratabound Mn samples of the Izu-Bonin arc system reflects the high temperature leaching of intermediate to acidic volcanic arc rocks. In the North Fiji Basin, Kuhn et al (2003) found that the OIBs were significantly enriched in Mo compared to N-MORB (more than two orders of magnitude) suggesting that they might represent the source of Mo in their hydrothermal precipitates. Although our results do not preclude a possible seawater contribution, we favor the leaching of volcanic rocks as an explanation for the high Mo concentrations in our samples.

5.3- Model

Regardless of a likely volcanic source for the metals in the Mn oxides at Utu Uli, Anakele and Utu Sega, there exist major differences in the mean concentrations of Ni, Co and Cu among deposits. Nickel is the dominant trace metal at Utu Uli (1.45 wt.% Ni) whereas Anakele Mn oxides samples are clearly controlled by copper (0.56 wt.% Cu) and Utu Sega Mn oxides are systematically enriched in cobalt (0.97 wt.% Co). Additionally, the mean Mo concentration is significantly higher in the Utu Uli mineralization (798 ppm; table 4) when compared to the mean for Anakele and Utu Sega (respectively 425 and 532 ppm; table 4). There may be several reasons that could explain the chemical variations among deposits: (i) mineralogical control, (ii) source rock composition, (iii) permeability of the volcanic edifice, rock/fluid ratios and mixing with seawater, (iv) depth and/or the longevity of the heat source, (v) the temperature, pH, Eh, salinity of the hydrothermal fluids. Massive precipitation of sulfides at depth has not contributed to the chemical signature recorded in our samples since this process would have led to the entrapment of Ni, Co, Cu and Mo in high-temperature sulfide phases. By contrast the difference in the proportion of Mn oxides may explain the higher mean Mo concentration obtained at Utu Uli with respect to Anakele. Indeed, when normalized for the higher Mn oxides fraction, mean concentrations of molybdenum turn out to be similar among the two sites. This mineralogical control by Mn oxides, however, does not explain the relatively low Mo contents in Utu Sega precipitates with respect to their high Mn concentration. N-MORBs were identified close to Utu Sega (e.g. Alofi ridge) whereas only OIB-like basalts and E-MORB were found near Utu Uli and Anakele (Labanieh et al., 2011). Considering that OIBs can be significantly enriched in Mo compared to N-MORB (Kuhn et al., 2003), lower molybdenum levels in Utu Sega Mn oxides might reflect a higher proportion of N-MORB as source components.

Although mineralogical control and/or various compositions of the source rocks may explain slight chemical variations of some trace elements such as Mo, we consider that it cannot explain the large variations of Ni, Co and Cu in the three mineralized sites (Table 4). The structure and mineralogical

composition at the millimeter scale reflect different pulses of hydrothermal fluids whereas variations at the micrometric to submillimetric scales are better explained by waxing and waning of a single hydrothermal pulse (Hein et al. 2008). It can be assumed from the chemical variations among the deposits as well as within a single mineralized site or an individual sample that hydrothermal phases and hydrothermal pulses within a single phase had different temperatures, Eh, pH and salinity. High cobalt concentrations in Mn oxides of the Mariana and Izu-Bonin arcs are considered as an evidence of a relatively high-temperature fluid (Hein et al., 2008). Mn oxides samples at Utu Sega are composed of the significant amount of 10 Å manganates that are still present 5 years after sampling. More stable 10 Å manganates are assumed to precipitate under high-temperature conditions (Usui et al., 1989). Moreover, chondrites-normalized REE patterns are characterized by a positive Eu anomaly which suggests (i) that the end-member fluid experienced temperature above 250°C (e.g. Craddock et al., 2010; Douville et al., 1999; Michard, 1989; Michard and Albarède, 1986) and (ii) a restricted mixing with seawater during precipitation of Mn oxides (by comparison with Mn oxides at Anakele and Utu Uli). Overall, these evidences suggest that Utu Sega Mn oxides formed at higher temperature than Utu Uli and Anakele Mn oxides.

In hydrothermal system, decreasing temperature and/or chloride concentrations can result in a decrease of the Co concentration in hydrothermal fluids (Liu et al., 2011). It is a consequence of the destabilization of tetrahedral complexes to octahedral species that favors the precipitation of cobalt as cattierite (CoS_2) (Liu et al., 2011). In the present study, neither SEM observations nor electron microprobe data support the presence of cattierite in Mn oxides with high levels of cobalt. An alternative hypothesis would be that cobalt species adsorb more readily onto Mn oxides than nickel or copper. Preferential sorption of cobalt over nickel onto manganese oxides has been shown by Kay et al. (2001) in both abiotic and biotic experiments. According to this study, the first Mn oxides to form (i.e. at the highest possible temperature and/or lowest possible Eh and/or pH) would be Co-rich and characterized by high Co/Ni ratio. At Utu Uli and Anakele, several samples display high cobalt contents (up to 2.24 wt.%). Electron microprobe chemical maps show a clear fractionation between cobalt on one hand and nickel (\pm copper) on the other (Fig. 11C). The alternation of high and low cobalt concentrations observed in the Mn oxides botryoids (Fig 11C) could reflect the waxing (high Co) and the waning stages (low Co) of the hydrothermal pulses. At a broader scale, we can hypothesize that the bulk samples with high cobalt contents suggest a closer proximity to the major hydrothermal up-flow zones. If we assume that the chemical variations of Co, Cu and Ni observed in the botryoids (from the core to the edge; Fig. 11C) mostly reflect the physical and chemical changes in the hydrothermal fluids, then nickel is thought to be fractionated from hydrothermal fluids at a lower temperature and/or higher Eh and/or pH (e.g. as a consequence of stronger mixing with seawater) than would cobalt. Mn oxide samples characterized by very high nickel concentrations

would therefore represent the distal part of high-temperature hydrothermal system. Finally, the large variation of nickel and cobalt recorded in our mineralized samples within a deposit (e.g. FU-DR01-07 and FU-DR01-08; Utu Uli; Table 1) could be the consequence of the evolution in space and time of temperature, pH and Eh within a single mineralized site.

5.3.1- Anakele and Utu Uli

The Utu Uli and Anakele Mn deposits lie on top of volcanic edifices and are intimately associated with basaltic pyroclastic rocks. The hydrothermal character of the mineralization is evident since Fe-Si-Mn precipitates are clearly different in morphology, microstructure, crystallinity, mineralogical and geochemical composition than those of hydrogenetic and diagenetic mineralization. Magmatic sills and intrusion of dikes within the volcanoes probably produced the hydrothermal circulation. Large volumes of seawater may have circulated through extensive conduits resulting from the high porosity of the host rocks. Major textural and mineralogical changes of the host rocks have been observed in several subsurface samples. Since pyroclast and volcanic glass degradation is enhanced with increased temperatures, the strong and pervasive alteration of the host rocks argue for the percolation of a high temperature fluid ($\geq 150^{\circ}\text{C}$) during waxing stages of some hydrothermal pulses (Hein et al., 2008). However direct contribution of CO_2 by magmatic fluids, though hypothetical, may have promoted the leaching of the volcanic rocks at relatively lower temperature (Escoube et al., 2015). Then, hot modified seawater generated by the convective hydrothermal circulation driven by heat of magma bodies is inferred to have leached the basaltic rocks which provided the trace elements (including metals) to the fluids.

The local geological setting (e.g. depth of mineralization, relationship with pyroclastic volcanoes, hotspots influence on the magmatic products) suggest that the first step of the hydrothermal activity at Utu Uli and Anakele might be similar to the hydrothermal activity identified at Loihi seamount. At Loihi, the warm (up to 55°C) vent solutions are enriched in Fe, Mn, Si, CH_4 , CO_2 and possibly Ni (Sedwick et al., 1992). According to Sedwick et al. (1994, 1992) the compositions of these warm fluids are consistent with the sub-seafloor mixing of a high-temperature ($>200^{\circ}\text{C}$) hydrothermal fluids with seawater together with the addition of magmatic volatiles (CO_2 and SO_2) (Wheat et al., 2000). High CO_2 results in low pH conditions ($\text{pH} < 5.5$) and high alkalinity which promotes alteration of the volcanic rocks (Escoube et al., 2015; Sedwick et al., 1992). The green, yellow orange to reddish deposits formed at or near the seafloor as the hydrothermal fluids mixed with seawater (De Carlo et al., 1983). Nontronite, Fe-montmorillonite, lepidocrocite and X-ray amorphous Fe oxides and silica are the main mineral phases identified (De Carlo et al., 1983). If we assume a similar process at Utu Uli and Anakele, Fe-rich smectite, iron oxyhydroxides and opal would have been the first mineral phases to precipitate. If the LT fluids were similar to those of Loihi, they would have been enriched in

Fe, Mn, Si and Ni relative to seawater and hydrothermal fluids from mid-ocean ridge (Sedwick et al., 1992). Decreasing of the hydrothermal activity could have driven the oxidation of Mn(II) on seafloor leading to the development of layered manganese crust. This crust has low to very low trace metals and probably formed by precipitation of manganese oxides in an open system where metals were massively lost in the water column. This widespread and ca. 2-cm-thick Mn layer might have sealed the hydrothermal system and trapped the metals-rich hydrothermal fluids (e.g. Fouquet et al., 1993) promoting their adsorption on Mn oxides. Successive hydrothermal pulses and related waning and waxing stages might have produced the textural (i.e. intercalation of AC, MC and C oxides) and geochemical (decoupling of Co, Cu and Ni) diversity of the cement-like Mn oxides; the Co-rich AC and MC oxides reflecting higher temperature hydrothermal pulses and Ni-rich MC and C Mn oxides reflecting lower temperature hydrothermal pulses. The Mn oxides progressively infilled pore spaces and replaced the Fe-rich smectite, eventually forming nearly pure Mn mineralization up to 10-cm-thick and strongly enriched in Ni and/or Cu and/or Co. Subsequent high-temperature hydrothermal stages led to a fracturing of the layered Mn crust and the precipitation the Fe-Si-rich crests and/or veins at the seafloor.

Processes at the subsurface level are still poorly known. However, high Ni, Co and Cu contents in the Mn oxides suggest that precipitation of massive HT sulfides bodies at depth was limited. Low barium and strontium concentrations compared to other hydrothermal Mn oxides deposits (Table 4) might reflect the precipitation of barite at depth. At Loihi, barite-rich sulfate mineralization with sulfides were sampled after the collapse of the summit crater in 1996 (Davis et al., 2003; Davis and Clague, 1998). Bulk composition of these hydrothermal samples shows high concentrations of Ba, Sr, Zn and Pb (Davis et al., 2003); these elements are systematically depleted in the Mn oxides at Utu Uli and Anakele. Even though further studies are required, precipitation of minor barite and zinc sulfide or sulfates at depth might explain the lack of major Ba, Sr, and Zn enrichment in the Mn oxides at Utu Uli and Anakele.

5.3.2- Utu Segá

Little is known about the local geology and the morphology of the mineralization at Utu Segá. From the dredge haul we may suppose that host rocks are mainly composed of strongly altered volcanic breccias and lavas and sediments. The structure, mineralogy and texture of the Mn oxide sample resemble the stratabound Mn oxide described by Hein et al. (2008, 1996b, 1990) in arc and intraplate settings. However, chemical data are significantly different than those reported for stratabound Mn deposits. Cobalt is highly enriched and REE chondrite-normalized patterns display a positive Eu anomaly, which is considered to be diagnostic of a high-temperature influence (e.g. Craddock et al.,

2010; Douville et al., 1999; Michard, 1989; Michard and Albarède, 1986). These evidences, coupled to the high stability of 10 Å manganates after 5 years which is characteristic of high temperature Mn mineralization (Usui et al., 1989), point to a precipitation close to the hydrothermal source. A more focused hydrothermal activity similar to that seen at the Lau basin deposits (i.e. Hine Hina and Vai Lili; Fouquet et al., 1993) might be proposed. However, at Lau basin precipitation of high-temperature sulfides in subsurface have precluded any Co, Ni and Cu enrichment in the Mn oxide crusts, which is obviously not the case at Utu Segá. Finally, the studied Mn oxides samples share common features with the stratabound Mn layers and Mn nodules of the Galicia Bank (González et al., 2016). These latters which exhibit high Co concentrations and strong europium positive anomalies (Table 4) are thought to be derived from metal-rich ascending hydrothermal fluids that leached the basement rocks and/or organic-matter-rich sediments (González et al., 2016). A potential on-land analog of Utu Segá deposit occurs in the Calatrava Volcanic Field (CVF; Spain) (Crespo et al., 1995; Crespo and Lunar, 1997). Mn-rich samples have high cobalt concentrations (up to 1.7 wt.%) and sometimes high Cu (up to 0.87 wt.%) and high Ni (up to 0.62 wt.%). Highest Co concentrations are recorded for samples with high Fe; however the iron oxides mineralization followed in time the deposition of Co-rich Mn oxides (Crespo et al., 1995). Crespo et al. (1995) and Crespo and Lunar, (1997) proposed a volcanogenic-hydrothermal origin for the mineralization. Metals were transported by epithermal hydrothermal solutions with high fO_2 and scavenged by Mn oxides in close proximity to the volcanism emission centers and normal faults.

Additional detailed studies (e.g. submersible dives) at Utu Segá are required to constrain the genetic model of this atypical type of mineralization.

5.4 Resources considerations

The mean average of nickel, copper and cobalt (Table 4) are 1 to 2 orders of magnitude greater than most hydrothermal manganese mineralization studied worldwide. Furthermore, the mean concentrations of base metals are similar if not greater than those reported for hydrogenetic crusts (Table 4). The Utu Uli deposit displays the most striking enrichment especially regarding the mean nickel concentration (> 1.45 wt.%) that overreach means nickel contents in nodules found in the Clarion-Clipperton zone.

Hydrothermal manganese deposits are commonly considered economically less important and only valuable as indicator for exploration for polymetallic sulfide (Usui and Someya, 1997). In regards to the estimated mineralized area (ca. 1.5km²), a mean thickness of ca. 5cm and the mean concentration of Mn, Ni, Co and Cu, Utu Uli and Anakele might hold respectively up to 38,200 t and 27,000 t Mn, 2200 t and 580 t Ni, 520 t and 450 t Co, 100 t and 840 t Cu.

Even though these calculations are subject to caution due to high uncertainties, these results highlight that in specific contexts, oceanic hydrothermal Mn-Fe-Si deposits may enclose significant amounts of metals. New exploration campaigns are now required to locate other deposits and to evaluate if this type of low-tonnage Mn deposits could provide a long-term potential resource.

5.5 Implications on the trace metal budgets of the ocean

Hydrothermal venting has long been recognized to provide significant fluxes of chemical to the ocean (e.g. Edmond et al., 1979) even if its impact on the chemical composition of seawater is still not well defined (Sander and Koschinsky, 2016). Low temperature venting account for significant portions of heat fluxes along mid-ocean ridge but are considered as a simple mixtures of bottom seawater and a high temperature end member (Wheat et al., 2000) with a relatively homogeneous composition and very low metal concentrations. Studies on diffuse venting at Loihi illustrate that low temperature hydrothermal fluids can have a wide range of compositions and possible impact on the fluxes of some elements (e.g. CO₂, Mg, sulfate, K; Wheat et al., 2000). In this study, we found low temperature Mn-Fe-Si mineralisation that precipitate form a Ni-, Co-, Cu-rich low temperature hydrothermal fluid. Loss of metals in the water column is expected in the first steps of the hydrothermal activity before the isolation of the system (see 5.3.1). A recent study (Atkins et al., 2014) shows that aging of metal-rich birnessite might provide a source for trace metals to seawater (e.g. nickel). Then, late release of metals to seawater might also occur long after the hydrothermal activity ceased. This type of metal-rich hydrothermal fluid and precipitates is not restricted to the studied area are since hydrothermal Mn mineralization with minor to major metal enrichments are known in continental margin (Gonzalez et al., 2016), hotspot (Hein et al., 1996; Moore and Vogt, 1976), arc (Hein et al., 2008, 1992) and back-arc (Kuhn et al., 2003) settings. Since low-temperature hydrothermal activity is difficult to detect using conventional sensors, we may hypothesize that this kind of processes could be widespread in deep-sea environments. Even though the impact on oceanic trace metals cycles is uncertain, the impact of metal-rich low temperature hydrothermal fluids and precipitates should be considered by future studies examining the biogeochemical cycle of metals in the ocean.

6. Conclusions

The Utu Uli, Anakele and Utu Sega deposits discovered during the FUTUNA cruise (2010) are unusual owing to their high concentrations in transition metals (i.e. Ni, Co, Cu). These deposits outcrop on top of the volcanoes and formed in close association with the volcanic facies. In-situ observations, mineralogical and geochemical studies clearly support a hydrothermal origin for the mineralization. The manganese mineralization occurs as massive layered crust and Mn-cement in strongly altered pyroclastic rocks, brecciated lavas and rarely sandstones. Relatively large hydrothermal cells (up to

hundreds of meters) developed within the highly porous volcanic edifices, driven by the heat from the magmatic dikes and sills. The widespread distribution of the Mn mineralization is most likely related to the high permeability of the host rocks and strong mixing of the hydrothermal fluids with seawater. Nickel, cobalt and copper enrichments are obviously controlled by the precipitation of 7 Å and 10 Å manganates. Several parameters might explain the enrichment of metals in our hydrothermal ferromanganese deposits: (i) lack of precipitation of HT massive sulfides at depths which would have retained Ni, Co and Cu (Glasby et al., 1997); (ii) entrapment of metals at subsurface level avoiding their loss in the water column (Fouquet et al., 1993); and (iii) the ability of birnessite and buserite/todorokite to scavenge Co, Ni, and Cu from solutions (Post, 1999). Metal loss in the water column during the first steps of the hydrothermal activity can account for the depleted character of the dense layered Mn crust which precipitates onto seafloor. We assume that this layer, which covers large areas at surface, formed a cap at the seawater/seafloor interface that eventually trapped the hydrothermal fluid (Fouquet et al., 1993). The isolation of the hydrothermal system led to the retention of Ni, Cu, and Co at subsurface level promoting their adsorption onto the manganese oxyhydroxides with cement texture. The large chemical variations of trace metals in Mn oxides among and within deposits most likely reflect changes of physical and chemical factors (e.g. T°, pH, Eh, salinity) of the hydrothermal fluids in space and time. Utu Uli and Anakele mineralization might be the result of the evolution of a hydrothermal activity similar to that presently occurring at Loihi seamount. Besides, the Co-rich Mn deposits of the Calatrava Volcanic Field (CVF; Spain) and the Co-rich nodules of the Galicia Bank (Gonzalez et al., 2016) are perhaps the most likely analogs to mineralization at Utu Sega. The CVF Mn-(Co) deposits formed in close proximity to Pliocene volcanic rocks. Metals were transported by epithermal hydrothermal solutions with high fO₂ and cobalt was strongly scavenged by Mn oxides (Crespo et al., 1995; Crespo and Lunar, 1997).

A recent study (Atkins et al., 2014) shows that aging of metal-rich birnessite might provide a source for trace metals to seawater (e.g. nickel). As a consequence, metals-rich low-temperature diffuse flow vents might represent a significant source of metals to the seawater via direct losses in the water column and/or indirect release during aging of enriched manganates. Given the occurrence of several Mn mineralization and LT hydrothermal fluids (Sakai et al., 1987) with minor to major metal enrichments in different settings (González et al., 2016; Hein et al., 2008, 1996, 1992; Kuhn et al., 2003; Moore and Vogt, 1976), and the fact that low-temperature hydrothermal activity is difficult to detect using conventional sensors, we suggest that this kind of processes could be widespread in deep-sea environments. In that case, the metal-rich low-temperature hydrothermal activity may be of major importance for future research on the net flux of hydrothermally derived trace metals (e.g. Ni, Co, Cu) to the open ocean.

Acknowledgment

The exploration cruise of the French EEZ of Wallis and Futuna during which studied deposits were discovered in 2010 was financed through a public/private consortium of the French state, Ifremer AMP, and BRGM on one side and the industrial groups Eramet, Technip and Areva. We thank the crews of R/V l'Atlante and Nautille HOV (Ifremer, France) and all participants of the FUTUNA cruise for their assistance at sea. A.S.Alix is thanks for the GIS data management and P.Fernagu is thanks for the preparation of polished sections.

Author contribution

Y.F. conceived the project and participated as chief scientist in the FUTUNA cruise (R/V L'Atalante). J.E., S.C. performed sample/chemical preparation and analyzed the samples (XRD, ED-XRF and WD-XRF). J.L. and E.P. analyzed the manganates (electron microprobe). E.P. wrote the article. All authors contributed to discussions, interpretation of the results and manuscript writing.

Competing financial interests

The authors declare no competing financial interests.

Bibliography

- Alibo, D.S., Nozaki, Y., 1999. Rare earth elements in seawater: particle association, shale-normalization, and Ce oxidation. *Geochim. Cosmochim. Acta* 63, 363–372. doi:10.1016/S0016-7037(98)00279-8
- Atkins, A.L., Shaw, S., Peacock, C.L., 2014. Nucleation and growth of todorokite from birnessite: Implications for trace-metal cycling in marine sediments. *Geochim. Cosmochim. Acta* 144, 109–125. doi:10.1016/j.gca.2014.08.014
- Bau, M., Schmidt, K., Koschinsky, A., Hein, J., Kuhn, T., Usui, A., 2014. Discriminating between different genetic types of marine ferro-manganese crusts and nodules based on rare earth elements and yttrium. *Chem. Geol.* 381, 1–9. doi:10.1016/j.chemgeo.2014.05.004
- Bonatti, E., Kraemer, T., Rydell, H., 1972. Classification and genesis of submarine iron-manganese deposits., in: Horn, D.R. (Ed.), *Ferromanganese Deposits of the Ocean Floor*. Seabed Assessment Program, IDOE, NSF, Washington D.C., USA, pp. 149–166.
- Burns, R.G., Burns, V.M., 1977. Chapter 7 Mineralogy, in: Glasby, G.P. (Ed.), *Elsevier Oceanography Series, Marine Manganese Deposits*. Elsevier, pp. 185–248.
- Choi, J.H., Hariya, Y., 1992. Geochemistry and depositional environment of Mn oxide deposits in the Tokoro Belt, northeastern Hokkaido, Japan. *Econ. Geol.* 87, 1265–1274. doi:10.2113/gsecongeo.87.5.1265
- Conly, A.G., Scott, S.D., Bellon, H., 2011. Metalliferous Manganese Oxide Mineralization Associated with the Boléo Cu-Co-Zn District, Mexico. *Econ. Geol.* 106, 1173–1196. doi:10.2113/econgeo.106.7.1173
- Craddock, P.R., Bach, W., Seewald, J.S., Rouxel, O.J., Reeves, E., Tivey, M.K., 2010. Rare earth element abundances in hydrothermal fluids from the Manus Basin, Papua New Guinea: Indicators of sub-seafloor hydrothermal processes in back-arc basins. *Geochim. Cosmochim. Acta* 74, 5494–5513. doi:10.1016/j.gca.2010.07.003
- Crespo, A., Lunar, R., 1997. Terrestrial hot-spring Co-rich Mn mineralization in the Pliocene-Quaternary Calatrava Region (central Spain). *Geol. Soc. Lond. Spec. Publ.* 119, 253–264. doi:10.1144/GSL.SP.1997.119.01.16
- Crespo, A., Lunar, R., Oyarzuc, R., Doblas, M., 1995. Unusual case of hot springs-related Co-rich Mn mineralization in central Spain; the Pliocene Calatrava deposits. *Econ. Geol.* 90, 433–437. doi:10.2113/gsecongeo.90.2.433
- Cronan, D.S., 1997. Some controls on the geochemical variability of manganese nodules with particular reference to the tropical South Pacific. *Geol. Soc. Lond. Spec. Publ.* 119, 139–151. doi:10.1144/GSL.SP.1997.119.01.10
- Davis, A.S., Clague, D.A., 1998. Changes in the hydrothermal system at Loihi Seamount after the formation of Pele's pit in 1996. *Geology* 26, 399–402. doi:10.1130/0091-7613(1998)026<0399:CITHSA>2.3.CO;2
- Davis, A.S., Clague, D.A., Zierenberg, R.A., Wheat, C.G., Cousens, B.L., 2003. Sulfide Formation Related to Changes in the Hydrothermal System on Loihi Seamount, Hawai'i, Following the Seismic Event in 1996. *Can. Mineral.* 41, 457–472. doi:10.2113/gscanmin.41.2.457
- De Carlo, E.H., McMurtry, G.M., Yeh, H.-W., 1983. Geochemistry of hydrothermal deposits from Loihi submarine volcano, Hawaii. *Earth Planet. Sci. Lett.* 66, 438–449. doi:10.1016/0012-821X(83)90157-7
- Douville, E., Bienvenu, P., Charlou, J.L., Donval, J.P., Fouquet, Y., Appriou, P., Gamo, T., 1999. Yttrium and rare earth elements in fluids from various deep-sea hydrothermal systems. *Geochim. Cosmochim. Acta* 63, 627–643. doi:10.1016/S0016-7037(99)00024-1
- Douville, E., Charlou, J.L., Oelkers, E.H., Bienvenu, P., Jove Colon, C.F., Donval, J.P., Fouquet, Y., Prieur, D., Appriou, P., 2002. The rainbow vent fluids (36°14'N, MAR): the influence of ultramafic rocks and phase separation on trace metal content in Mid-Atlantic Ridge hydrothermal fluids. *Chem. Geol.* 184, 37–48. doi:10.1016/S0009-2541(01)00351-5

- Dymond, J., Lyle, M., Finney, B., Piper, D.Z., Murphy, K., Conard, R., Pisias, N., 1984. Ferromanganese nodules from MANOP Sites H, S, and R—Control of mineralogical and chemical composition by multiple accretionary processes. *Geochim. Cosmochim. Acta* 48, 931–949. doi:10.1016/0016-7037(84)90186-8
- Edmond, J.M., Measures, C., Mangum, B., Grant, B., Sclater, F.R., Collier, R., Hudson, A., Gordon, L.I., Corliss, J.B., 1979. On the formation of metal-rich deposits at ridge crests. *Earth Planet. Sci. Lett.* 46, 19–30. doi:10.1016/0012-821X(79)90062-1
- Escoube, R., Rouxel, O.J., Edwards, K., Glazer, B., Donard, O.F.X., 2015. Coupled Ge/Si and Ge isotope ratios as geochemical tracers of seafloor hydrothermal systems: Case studies at Loihi Seamount and East Pacific Rise 9°50'N. *Geochim. Cosmochim. Acta* 167, 93–112. doi:10.1016/j.gca.2015.06.025
- Fouquet, Y., Alix, A.-S., Birot, D., Chéron, S., Charlou, J.L., Donval, J.-P., Etoubleau, J., Germain, Y., Guillou, M., Guerin, C., Guyader, V., Konn, C., Labanieh, S., Pelleter, E., Pierre, D., Dupré, S., Scalabrin, C., Cambon, M.-A., Menot, L., Pradillon, F., Chazot, G., Dymont, J., Sztikar, F., Gouin, J., 2015. Discovery of extensive hydrothermal fields in the Wallis and Futuna back-arc environment (SW Pacific), in: André-Mayer, A.-S., Cathelineau, M., Muchez, P., Pirard, E., Sindern, S. (Eds.), *Mineral Resources in a Sustainable World, Proceedings of the 13th Biennial SGA Meeting, 24-27 August 2015*. pp. 1223–1226.
- Fouquet, Y., Cambon, P., Etoubleau, J., Charlou, J.L., Ondréas, H., Barriga, F.J.A.S., Cherkashov, G., Semkova, T., Poroshina, I., Bohn, M., Donval, J.P., Henry, K., Murphy, P., Rouxel, O., 2010. Geodiversity of Hydrothermal Processes Along the Mid-Atlantic Ridge and Ultramafic-Hosted Mineralization: a New Type Of Oceanic Cu-Zn-Co-Au Volcanogenic Massive Sulfide Deposit, in: Rona, P.A., Devey, C.W., Dymont, J., Murton, B.J. (Eds.), *Diversity Of Hydrothermal Systems On Slow Spreading Ocean Ridges*. American Geophysical Union, pp. 321–367.
- Fouquet, Y., Stackelberg, U. von, Charlou, J.L., Erzinger, J., Herzig, P.M., Muehe, R., Wiedicke, M., 1993. Metallogenesis in back-arc environments; the Lau Basin example. *Econ. Geol.* 88, 2154–2181. doi:10.2113/gsecongeo.88.8.2154
- Glasby, G.P., Stüben, D., Jeschke, G., Stoffers, P., Garbe-Schönberg, C.D., 1997. A model for the formation of hydrothermal manganese crusts from the Pitcairn Island hotspot. *Geochim. Cosmochim. Acta* 61, 4583–4597. doi:10.1016/s0016-7037(97)00262-7
- González, F.J., Somoza, L., Hein, J.R., Medialdea, T., León, R., Urgorri, V., Reyes, J., Martín-Rubí, J.A., 2016. Phosphorites, Co-rich Mn nodules, and Fe-Mn crusts from Galicia Bank, NE Atlantic: Reflections of Cenozoic tectonics and paleoceanography. *Geochem. Geophys. Geosystems* 17, 346–374. doi:10.1002/2015GC005861
- Goto, K.T., Shimoda, G., Anbar, A.D., Gordon, G.W., Harigane, Y., Senda, R., Suzuki, K., 2015. Molybdenum isotopes in hydrothermal manganese crust from the Ryukyu arc system: Implications for the source of molybdenum. *Mar. Geol.* 369, 91–99. doi:10.1016/j.margeo.2015.08.007
- Hein, J.R., Ahn, J.-H., Wong, J.C., Kang, J.-K., Smith, V.K., Yoon, S.-H., d'Angelo, W.M., Yoo, S.-O., Gibbs, A.E., Kim, H.-J., Quinterno, P.J., Jung, M.-Y., Davis, A.S., Park, B.-K., Gillison, J.R., Marlow, M.S., Schulz, M.S., Siems, D.F., Taggart, J.E., Rait, N., Pickthorn, L.G., Malcolm, M.J., Kavulak, M.G., Yeh, H.-W., Mann, D.M., Noble, M.A., Riddle, G.O., Roushey, B.H., Smith, H., 1992. Geology, geophysics, geochemistry, and deep-sea mineral deposits, Federated States of Micronesia; KORDI-USGS R.V. Farnella Cruise F11-90-CP (USGS Numbered Series No. 92–218), Open-File Report. U.S. Geological Survey,
- Hein, J.R., Gibbs, A.E., Clague, D.A., Torresan, M., 1996. Hydrothermal mineralization along submarine rift zones, Hawaii. *Mar. Georesources Geotechnol.* 14, 177–203.
- Hein, J.R., Koschinsky, A., Bau, M., Manheim, F.T., Kang, J.-K., Roberts, L., 2000. Cobalt-rich ferromanganese crusts in the Pacific, in: *Handbook of Marine Mineral Deposits*. CRC Press, pp. 239–279.

- Hein, J.R., Koschinsky, A., Halbach, P., Manheim, F.T., Bau, M., Kang, J.-K., Lubick, N., 1997. Iron and manganese oxide mineralization in the Pacific. *Geol. Soc. Lond. Spec. Publ.* 119, 123–138. doi:10.1144/GSL.SP.1997.119.01.09
- Hein, J.R., Mizell, K., Koschinsky, A., Conrad, T.A., 2013. Deep-ocean mineral deposits as a source of critical metals for high- and green-technology applications: Comparison with land-based resources. *Ore Geol. Rev.* 51, 1–14. doi:10.1016/j.oregeorev.2012.12.001
- Hein, J.R., Schulz, M.S., Dunham, R.E., Stern, R.J., Bloomer, S.H., 2008. Diffuse flow hydrothermal manganese mineralization along the active Mariana and southern Izu-Bonin arc system, western Pacific. *J Geophys Res* 113, B08S14. doi:10.1029/2007jb005432
- Hein, J.R., Schulz, M.S., Kang, J.-K., 1990. Insular and Submarine Ferromanganese Mineralization of the Tonga-Lau Region. *Mar. Min.* 9, 305–354.
- Hein, J.R., Spinardi, F., Okamoto, N., Mizell, K., Thorburn, D., Tawake, A., 2015. Critical metals in manganese nodules from the Cook Islands EEZ, abundances and distributions. *Ore Geol. Rev.* 68, 97–116. doi:10.1016/j.oregeorev.2014.12.011
- Kay, J.T., Conklin, M.H., Fuller, C.C., O'Day, P.A., 2001. Processes of Nickel and Cobalt Uptake by a Manganese Oxide Forming Sediment in Pinal Creek, Globe Mining District, Arizona. *Environ. Sci. Technol.* 35, 4719–4725. doi:10.1021/es010514d
- Krasnov, S.G., Cherkashev, G.A., Stepanova, T.V., Batuyev, B.N., Krotov, A.G., Malin, B.V., Maslov, M.N., Markov, V.F., Poroshina, I.M., Samovarov, M.S., Ashadze, A.M., Lazareva, L.I., Ermolayev, I.K., 1995. Detailed geological studies of hydrothermal fields in the North Atlantic. *Geol. Soc. Lond. Spec. Publ.* 87, 43–64. doi:10.1144/GSL.SP.1995.087.01.05
- Krauskopf, K.B., 1957. Separation of manganese from iron in sedimentary processes. *Geochim. Cosmochim. Acta* 12, 61–84. doi:10.1016/0016-7037(57)90018-2
- Kuhn, T., Bau, M., Blum, N., Halbach, P., 1998. Origin of negative Ce anomalies in mixed hydrothermal–hydrogenetic Fe–Mn crusts from the Central Indian Ridge. *Earth Planet. Sci. Lett.* 163, 207–220. doi:10.1016/S0012-821X(98)00188-5
- Kuhn, T., Bostick, B.C., Koschinsky, A., Halbach, P., Fendorf, S., 2003. Enrichment of Mo in hydrothermal Mn precipitates: possible Mo sources, formation process and phase associations. *Chem. Geol.* 199, 29–43. doi:10.1016/S0009-2541(03)00054-8
- Labanieh, S., Chazot, G., Etoubleau, J., Fouquet, Y., Dosso, L., Hemond, C., 2011. Origin of the Seamounts Near Futuna Island, SW Pacific. *Mineral. Mag.* 75, 1261.
- Liu, W., Borg, S.J., Testemale, D., Etschmann, B., Hazemann, J.-L., Brugger, J., 2011. Speciation and thermodynamic properties for cobalt chloride complexes in hydrothermal fluids at 35–440 °C and 600 bar: An in-situ XAS study. *Geochim. Cosmochim. Acta* 75, 1227–1248. doi:10.1016/j.gca.2010.12.002
- Manheim, F.T., Lanebostwick, C.M., 1988. COBALT IN FERROMANGANESE CRUSTS AS A MONITOR OF HYDROTHERMAL DISCHARGE ON THE PACIFIC SEA-FLOOR. *Nature* 335, 59–62.
- Michard, A., 1989. Rare earth element systematics in hydrothermal fluids. *Geochim. Cosmochim. Acta* 53, 745–750. doi:10.1016/0016-7037(89)90017-3
- Michard, A., Albarède, F., 1986. The REE content of some hydrothermal fluids. *Chem. Geol.* 55, 51–60. doi:10.1016/0009-2541(86)90127-0
- Moorby, S.A., Cronan, D.S., Glasby, G.P., 1984. Geochemistry of hydrothermal Mn-oxide deposits from the S.W. Pacific island arc. *Geochim. Cosmochim. Acta* 48, 433–441. doi:10.1016/0016-7037(84)90272-2
- Moore, W.S., Vogt, P.R., 1976. Hydrothermal manganese crusts from two sites near the Galapagos spreading axis. *Earth Planet. Sci. Lett.* 29, 349–356. doi:10.1016/0012-821X(76)90139-4
- Nicholson, K., 1992. Contrasting mineralogical-geochemical signatures of manganese oxides; guides to metallogenesis. *Econ. Geol.* 87, 1253–1264. doi:10.2113/gsecongeo.87.5.1253
- Pelletier, B., Lagabrielle, Y., Benoit, M., Cabioch, G., Calmant, S., Garel, E., Guivel, C., 2001. Newly identified segments of the Pacific–Australia plate boundary along the North Fiji transform zone. *Earth Planet. Sci. Lett.* 193, 347–358. doi:10.1016/S0012-821X(01)00522-2

- Post, J.E., 1999. Manganese oxide minerals: Crystal structures and economic and environmental significance. *Proc. Natl. Acad. Sci.* 96, 3447–3454. doi:10.1073/pnas.96.7.3447
- Pouchou, J.L., Pichoir, F., 1988. A simplified version of the “PAP” model for matrix corrections in EPMA. *Microbeam Anal.* 315–138.
- Rogers, T.D.S., Hodkinson, R.A., Cronan, D.S., 2001. Hydrothermal Manganese Deposits from the Tonga-Kermadec Ridge and Lau Basin Region, Southwest Pacific. *Mar. Georesources Geotechnol.* 19, 245–268. doi:10.1080/106411901753335326
- Sakai, H., Tsubota, H., Nakai, T., Ishibashi, J., Akagi, T., Gamo, T., Tilbrook, B., Igarashi, G., Kodera, M., Shitashima, K., Nakamura, S., Fujioka, K., Watanabe, M., McMurty, G., Malahoff, A., Ozima, M., 1987. Hydrothermal activity on the summit of Loihi Seamount, Hawaii. *Geochem. J.* 21, 11–21. doi:10.2343/geochemj.21.11
- Sander, S.G., Koschinsky, A., 2016. The Export of Iron and Other Trace Metals from Hydrothermal Vents and the Impact on Their Marine Biogeochemical Cycle, in: Demina, L.L., Galkin, S.V. (Eds.), *Trace Metal Biogeochemistry and Ecology of Deep-Sea Hydrothermal Vent Systems, The Handbook of Environmental Chemistry*. Springer International Publishing, pp. 9–24.
- Sedwick, P.N., McMurty, G.M., Hilton, D.R., Goff, F., 1994. Carbon dioxide and helium in hydrothermal fluids from Loihi Seamount, Hawaii, USA: Temporal variability and implications for the release of mantle volatiles. *Geochim. Cosmochim. Acta* 58, 1219–1227. doi:10.1016/0016-7037(94)90587-8
- Sedwick, P.N., McMurty, G.M., Macdougall, J.D., 1992. Chemistry of hydrothermal solutions from Pele’s Vents, Loihi Seamount, Hawaii. *Geochim. Cosmochim. Acta* 56, 3643–3667. doi:10.1016/0016-7037(92)90159-G
- Sun, S.–., McDonough, W.F., 1989. Chemical and isotopic systematics of oceanic basalts: implications for mantle composition and processes. *Geol. Soc. Lond. Spec. Publ.* 42, 313–345. doi:10.1144/GSL.SP.1989.042.01.19
- Toth, J.R., 1980. Deposition of submarine crusts rich in manganese and iron. *Geol. Soc. Am. Bull.* 91, 44–54. doi:10.1130/0016-7606(1980)91<44:DOSCRI>2.0.CO;2
- Usui, A., Mellin, T.A., Nohara, M., Yuasa, M., 1989. Structural stability of marine 10 Å manganates from the Ogasawara (Bonin) Arc: Implication for low-temperature hydrothermal activity. *Mar. Geol.* 86, 41–56. doi:10.1016/0025-3227(89)90017-0
- Usui, A., Someya, M., 1997. Distribution and composition of marine hydrogenetic and hydrothermal manganese deposits in the northwest Pacific. *Geol. Soc. Lond. Spec. Publ.* 119, 177–198. doi:10.1144/GSL.SP.1997.119.01.12
- Wheat, C.G., Jannasch, H.W., Plant, J.N., Moyer, C.L., Sansone, F.J., McMurty, G.M., 2000. Continuous sampling of hydrothermal fluids from Loihi Seamount after the 1996 event. *J. Geophys. Res. Solid Earth* 105, 19353–19367. doi:10.1029/2000JB900088

Figures captions

Fig. 1: A. Main geodynamic features of the South-West Pacific region and localization of the studied area (B); B. Localization of the Utu Uli, Anakele and Utu Sega ferromanganese deposits (Wallis and Futuna region, SW-Pacific).

Fig. 2: Bathymetric maps of the three Mn deposits. See location in Fig. 1. A. Bathymetric map of Utu Uli deposit; purple line and red line correspond respectively to the tracks of dive FU-PL08 and dive FU-PL09. B. Bathymetric map of Anakele deposit; purple line corresponds to the tracks of dive FU-PL10. C. Bathymetric map of Utu Sega deposit. Dot black lines are the tracks of dredge hauls; white stars are the location of the samples collected during dive operations; white dot lines represent the extent of the Mn mineralization.

Fig. 3: Frame captures from HOV Nautila Dive FU-PL08, FU-PL09 and FU-PL10 video. A. Layered and massive Mn oxide crust; the surface is commonly fractured like a bread crust (Utu Uli). B. Mn mineralization crosscut by Fe-Si-rich crests composed of amorphous iron oxyhydroxides and opal (Utu Uli). C. Large Fe-Si-rich crest with worm tubes on top (Utu Uli). D. Iron oxides-rich layer outcropping beneath a 3 to 5-cm-thick Mn crust (Anakele). E. Mn crust with a granular texture overlying iron oxides and nontronite (Anakele). F. Fe-Si-rich mineralization that precipitates through fractures in thick (≥ 10 cm) Mn crust (Anakele).

Fig. 4: A. Sample FU-DR01-03 (Utu Uli) composed of Mn-cemented breccia covered by a 2-cm-thick massive and layered Mn crust. B. Sample of an iron and silica-rich crest that crosscut the manganese mineralization at surface (FU-PL08-04; Utu Uli). C. Mn oxide cemented pyroclastic breccia (FU-PL08-03; Utu Uli); pyroclasts are fully altered in a mixture of nontronite, Fe oxides and Mn oxides. D. Mn-Fe-Si cemented pyroclastic breccia with a striking compositional layering; from top to bottom: Mn oxides, iron oxides and green nontronite; Alt. B: altered basaltic pyroclast. E. Stratabound Mn oxide sample (FU-DR15-10) characterized by a lower part with massive structure and an upper part composed of alternation of dense and porous layers. F. Stratabound Mn oxide bed composed of several metallic gray layers (FU-DR22-02; Utu Sega).

Fig. 5: Polished section photomicrographs. A. Dense Mn layer composed of laminated and coalescent botryoids (Layered Mn crust, FU-DR01-03). B. Radially oriented Mn oxides growing in open spaces and characterized by different mineral-size classes (Mn-cemented pyroclastic breccia, FU-DR01-03). C and D. Radial-fibrous and spherulitic Mn oxides growing in pore spaces and at the expense of nontronite clasts (Mn-cemented pyroclastic breccia, FU-DR01-03); reflected (Fig. 5C) and polarized reflected light (Fig. 5D). E. Radial-fibrous Mn oxides with crystallites up to 600 μm in size

(Stratabound Mn oxide sample, FU-DR15-10). F. Scallop-like texture (Stratabound Mn oxide sample, Fu-DR22-03). AC: amorphous cryptocrystalline oxides; M: microcrystalline oxides; C: crystalline oxides.

Fig. 6. Scanning electron microscope photomicrographs. A. Surface of the massive and dense layered Mn crust (FU-DR01-03). B. Coalescent botryoids forming a columnar-like structure (FU-DR01-07). C. Close-up of a well-crystallized botryoid composed of very thin blade-like crystals of manganates (FU-DR01-03). D. Backscattered electron image showing alternation of amorphous cryptocrystalline, microcrystalline and crystalline Mn oxides (FU-PL08-02). E. Secondary electron image of well-crystallized manganates (todorokite) with blade-like structure (FU-DR15-10). F. Backscattered electron image of large todorkite crystals underlying several Mn oxide botryoids; darker BSE signal of crystallites and microcrystallites in the botryoids is due to epoxy resin (FU-DR15-10).

Fig. 7. Fe-Mn-(Si) \times 2 ternary diagram showing the composition of ferromanganese precipitates from Utu Uli (dark grey crosses), Anakele (light grey crosses) and Utu Sega (black circles).; the dot gray line corresponds to a mixing between pure Mn oxide and ideal composition of nontronite; the black dot line corresponds to mixing line between pure Mn oxide and a mean basalt composition of the studied area.

Fig. 8. A. Co-Ni-Cu ternary diagram showing the compositional difference of trace metals among the Mn deposits. B. Mn/(Mn+Fe+Si) versus Ni+Co+Cu concentrations (in wt.%) for data samples. C. Mn/(Mn+Fe+Si) versus Ni concentratins (in wt.%); At Utu Uli, nickel is clearly controlled by the manganates. D. Mn/(Mn+Fe+Si) versus Co concentrations (in wt.%) for data samples; several mineralized samples at Utu Uli and Anakele support some affinity between Co and manganates; At Utu Sega Co is clearly controlled by the manganates. E. Mn/(Mn+Fe+Si) versus Cu concentrations (in wt.%) for data samples; Only Anakele samples display a significant correlation between Cu and high Mn concentrations. F. Mn/(Mn+Fe+Si) versus Cu concentrations (in wt.%) for data sample. Same legend as Fig. 7.

Fig. 9. Chondrite-normalized (Sun and McDonough, 1989) REE plots for Utu Uli (a), Anakele (b), Utu Sega (c) Mn oxides; (d) REE patterns of Pacific seawater (1000 mbsfl; Alibo and Nozaki, 1999) and selected Pacific HT hydrothermal fluids (PacManus and Vai Laili; Douville et al., 1999).

Fig. 10. Fe-Mn-(Co+Ni+Cu) \times 10 ternary diagram (Bonatti et al. 1972); same legend as Fig. 7.

Fig. 11. Electron microprobe chemical maps of the layered massive crust (A; FU-DR01-03), Mn-cemented pyroclastic breccia (B; FU-DR01-03) and stratabound Mn oxide sample (C; FU-DR15-10). Red circles in B highlight area of nontronite replacement or the presence of residual signature of

nontronite in Mn oxide. Red circle in C shows an antipathetic relationship between Co in one hand and Cu and Ni in the other.

ACCEPTED MANUSCRIPT

Tables captions

Table 1. Chemical composition of bulk hydrothermal Fe-Mn-Si samples of Utu Uli, Anakele and Utu Sega.

Table 2. Rare earth elements composition of 15 hydrothermal Mn samples.

$$Ce/Ce^* : \frac{Ce}{Ce^*} = \frac{Ce_n}{\sqrt{(La_n.Pr_n)}} ; Eu/Eu^* : \frac{Eu}{Eu^*} = \frac{Eu_n}{\sqrt{(Sm_n.Gd_n)}}$$

Ce_{xs}: Cerium excess; GR: Growth rates in mm.Ma⁻¹

Table 3. Selected electron microprobe spot analyses of Mn oxides (CAMECA SX100, Microsonde Ouest, Brest).

Titanium was systematically below the detection limit; '-' below detection limit; C: Crystallites; MC: Microcrystallites; AC: Amorphous cryptocrystalline oxides; MC*: analyses of microcrystallites of the uppermost layered and massive crust

Table 4. Comparison of mean bulk composition of Utu Uli, Anakele and Utu Sega deposits with Fe-Mn deposits from the Pacific.

Galicja Bank*: one stratabound crust (DRR41-1B) and three Co-rich hydrothermal Mn nodules (DRR81-1, DRR21-1 and DRR21-2)

Pb**: n=14 (Utu Uli), n=7 (Anakele) and n=1 (Utu Sega)

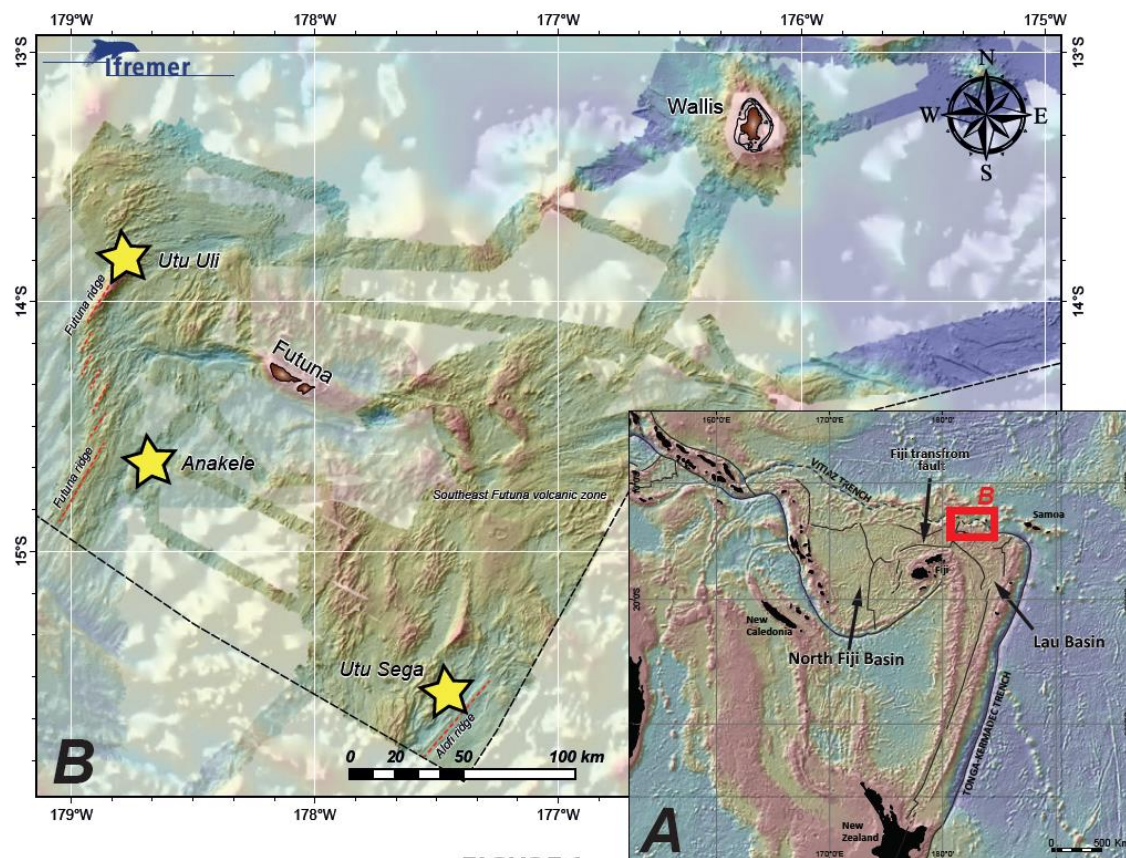


FIGURE 1

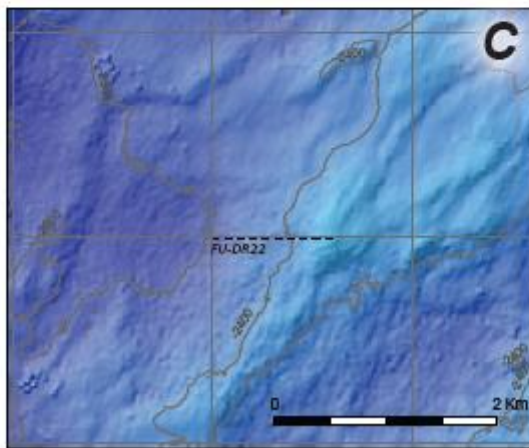
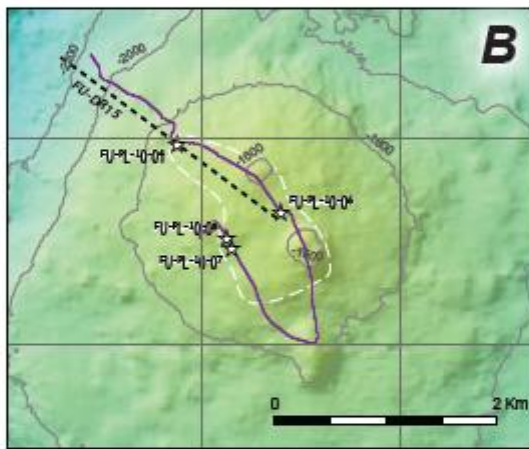
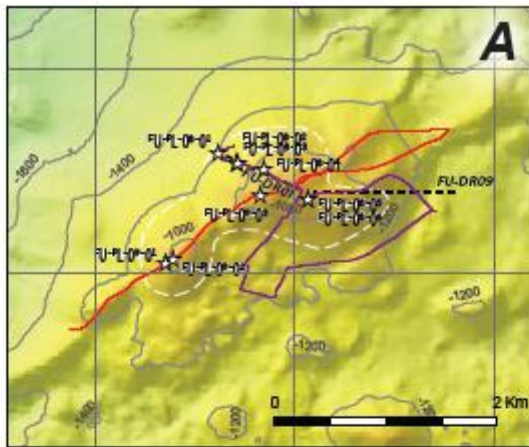


FIGURE 2

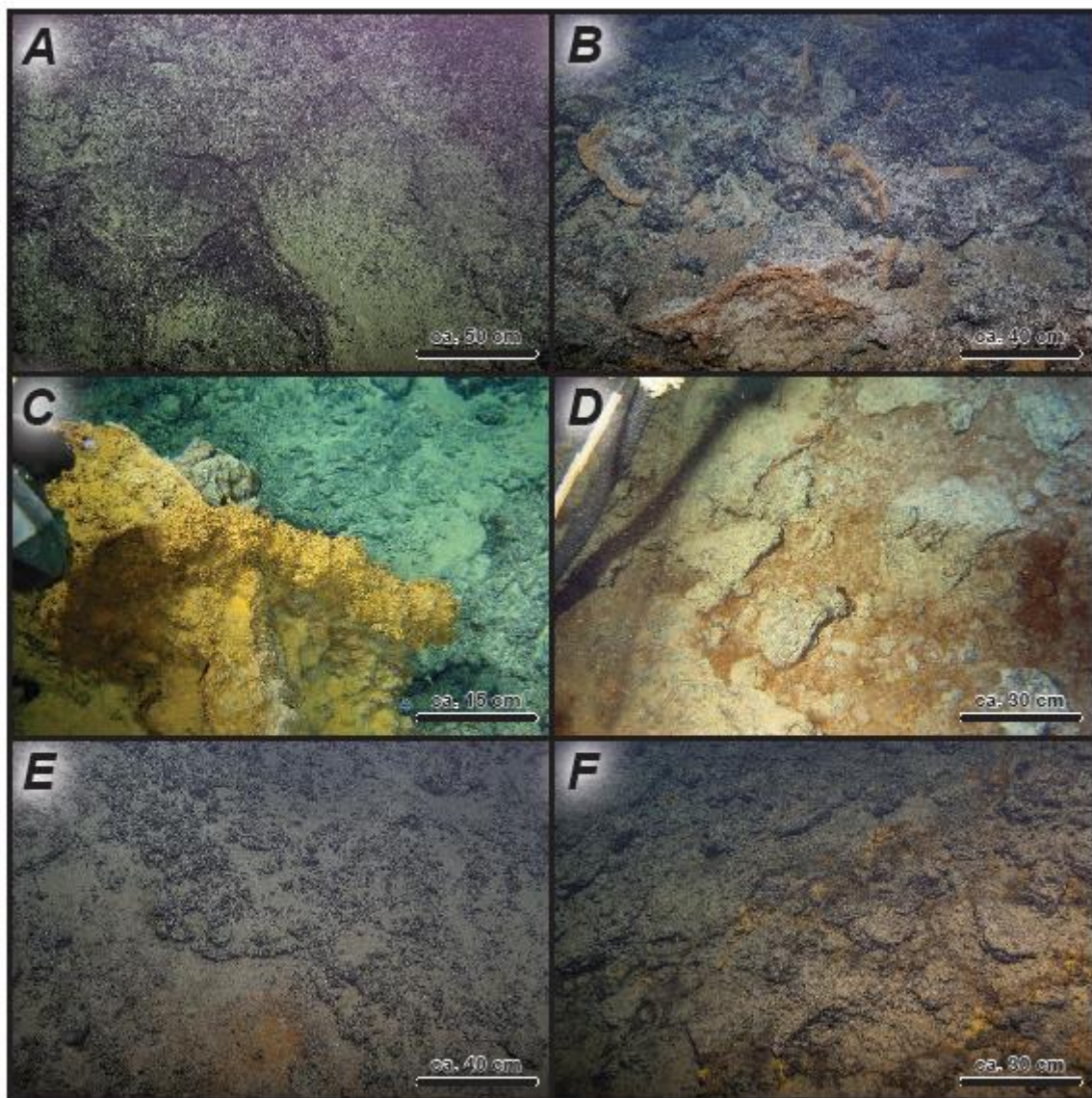


FIGURE 3

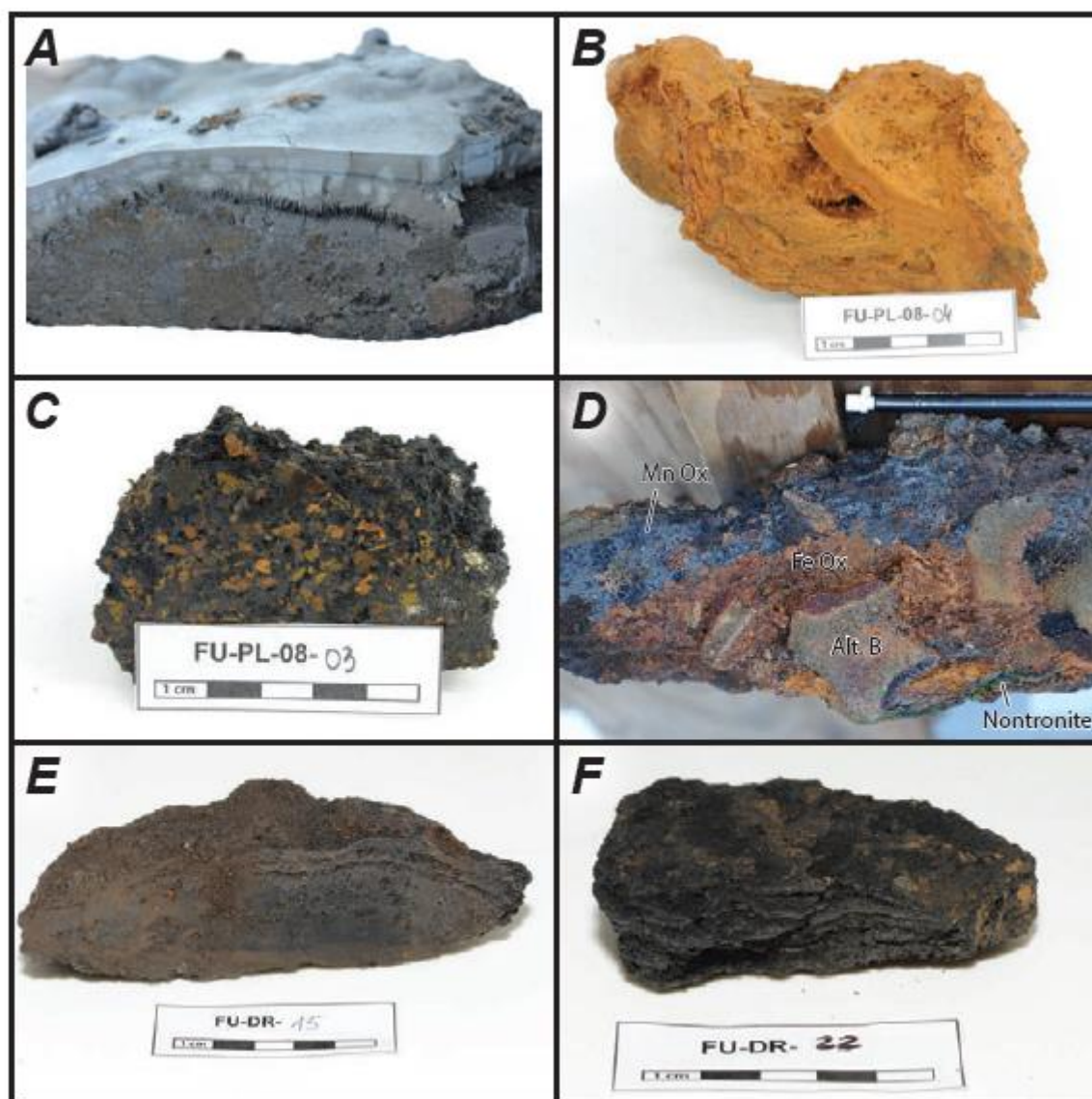


FIGURE 4

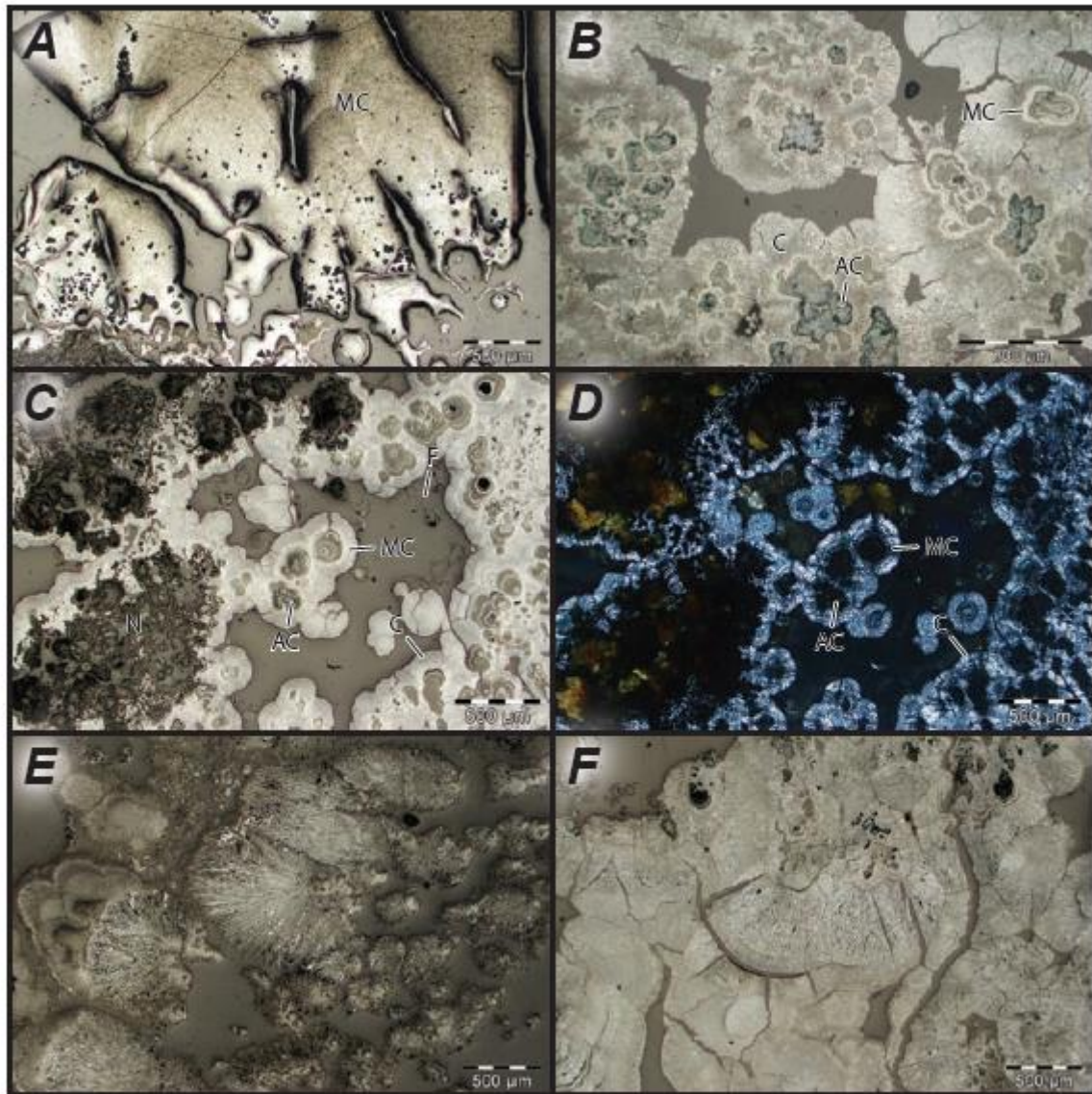


FIGURE 5

X

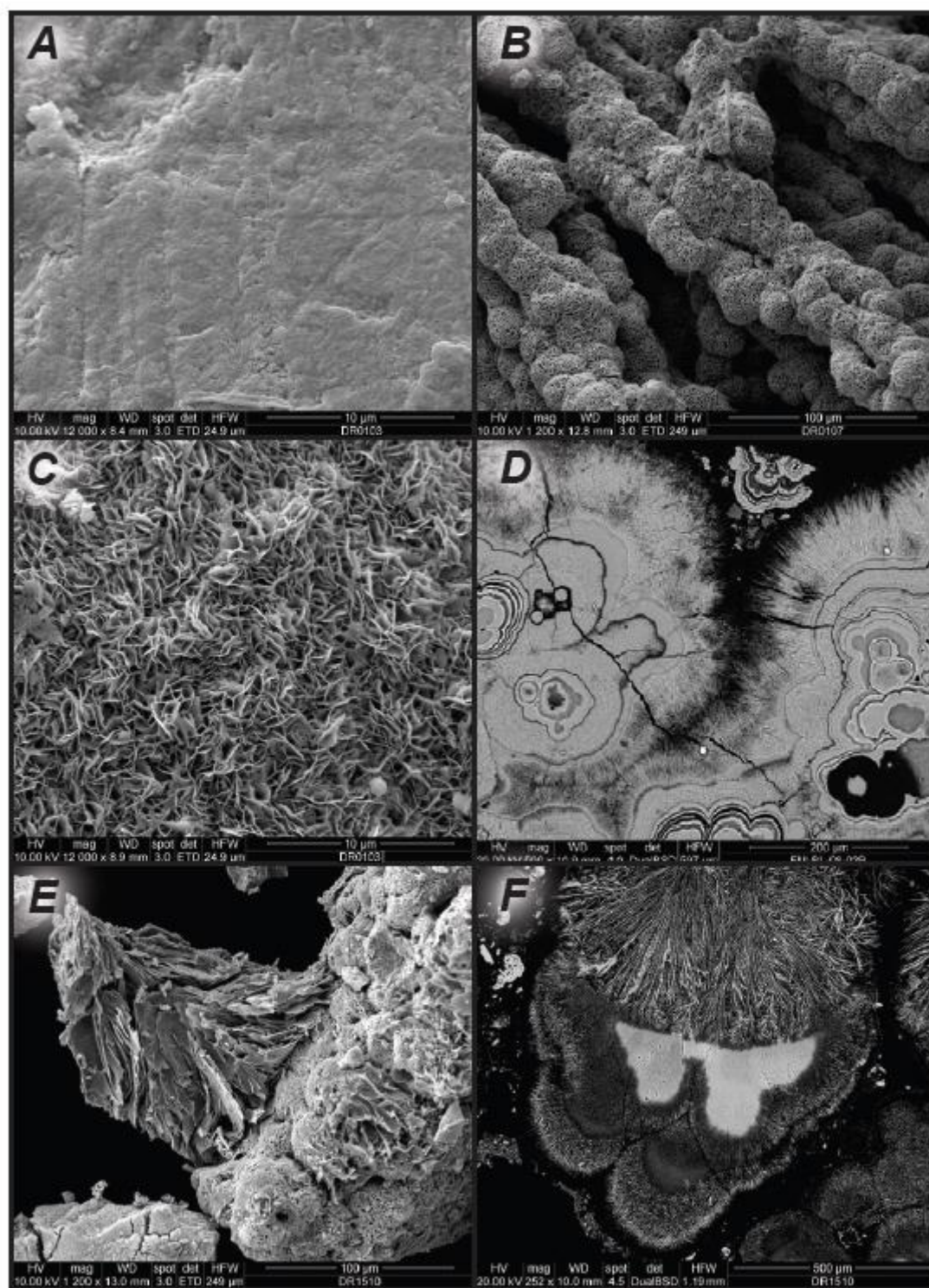
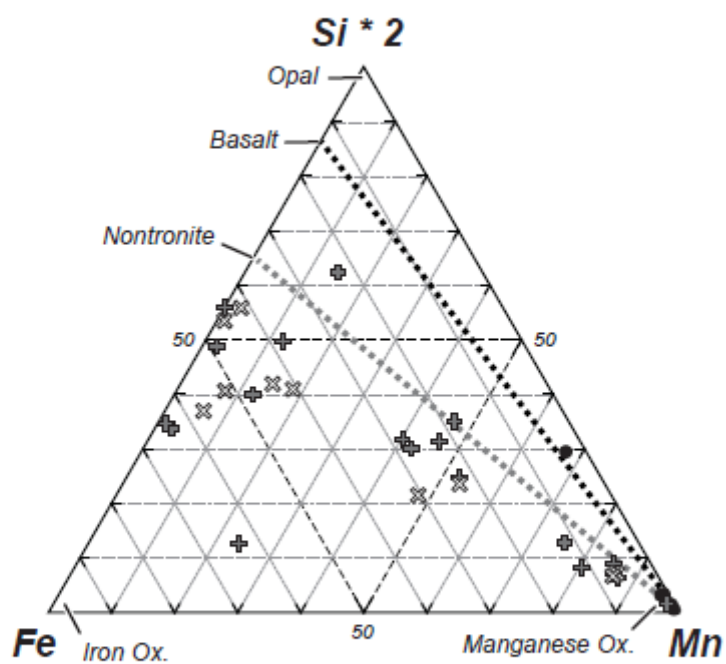


FIGURE 6

**FIGURE 7**

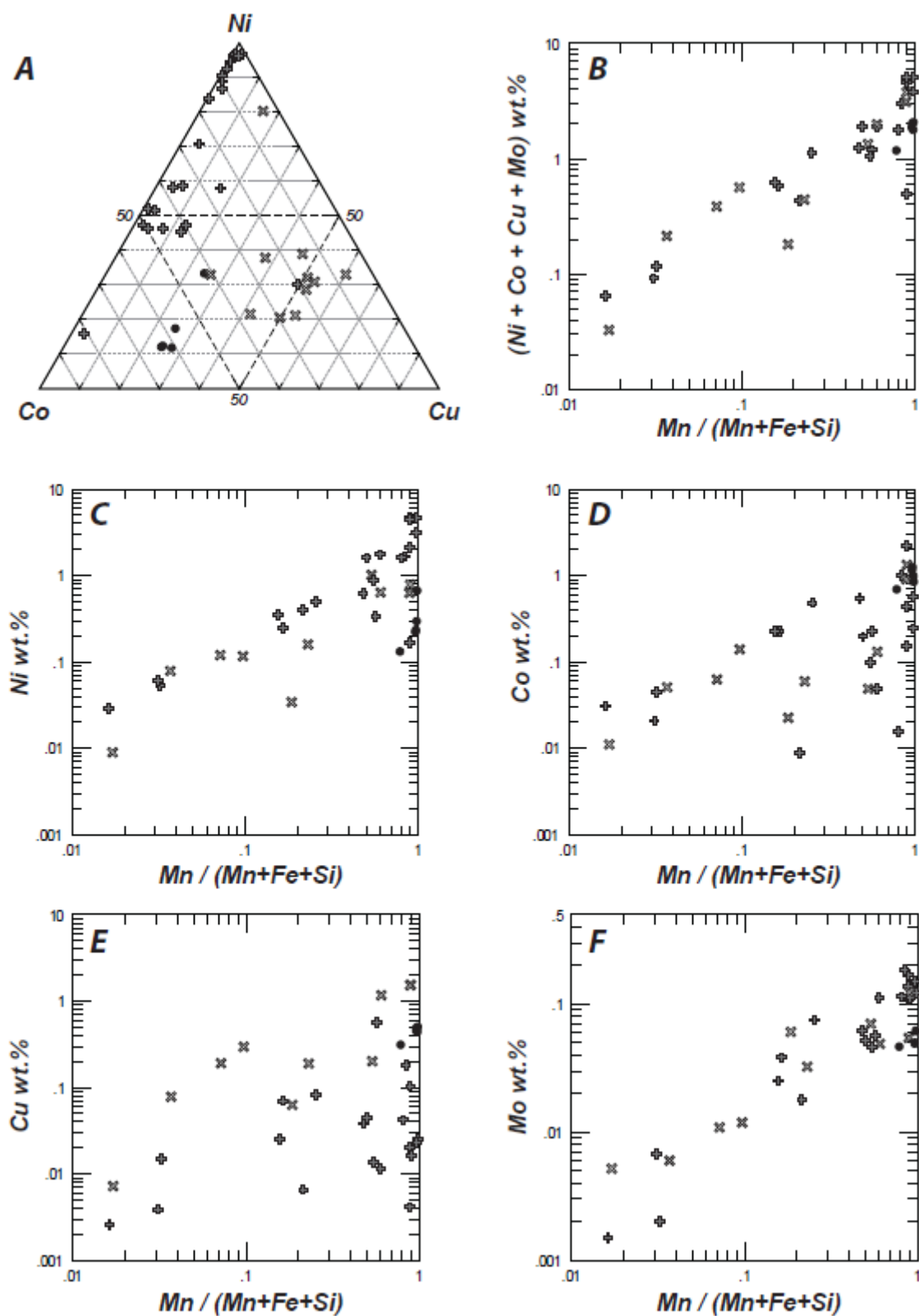


FIGURE 8

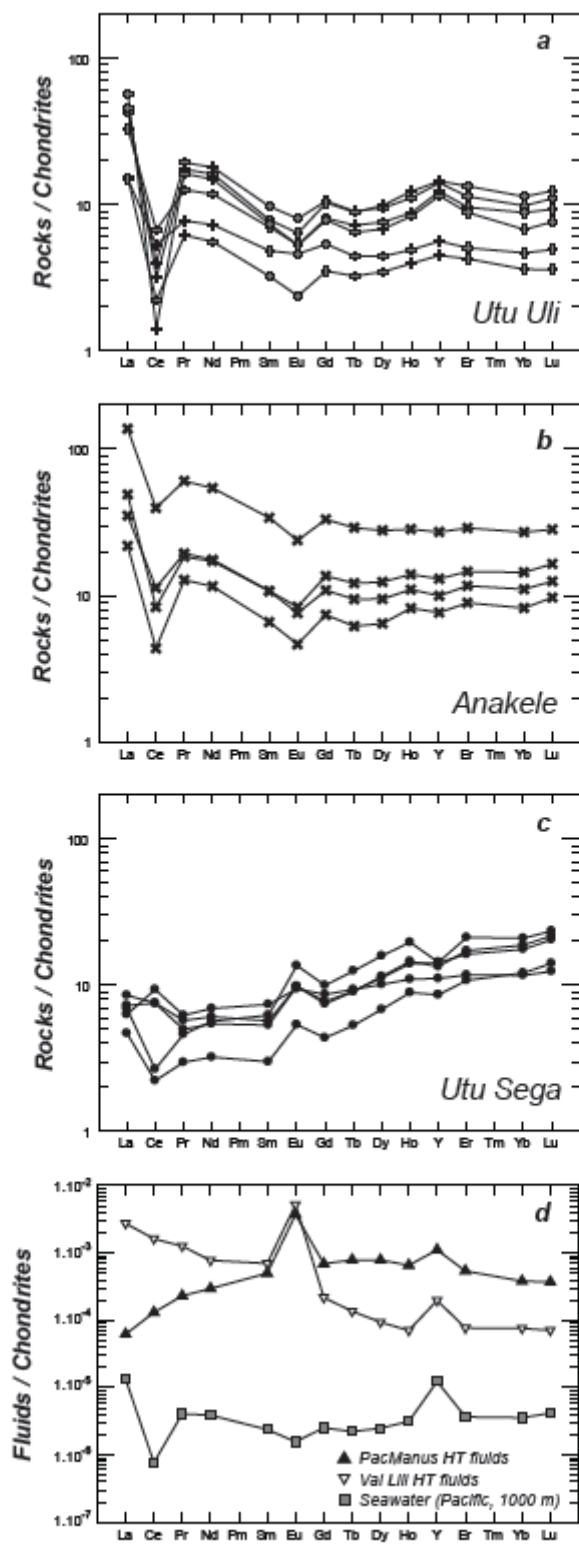
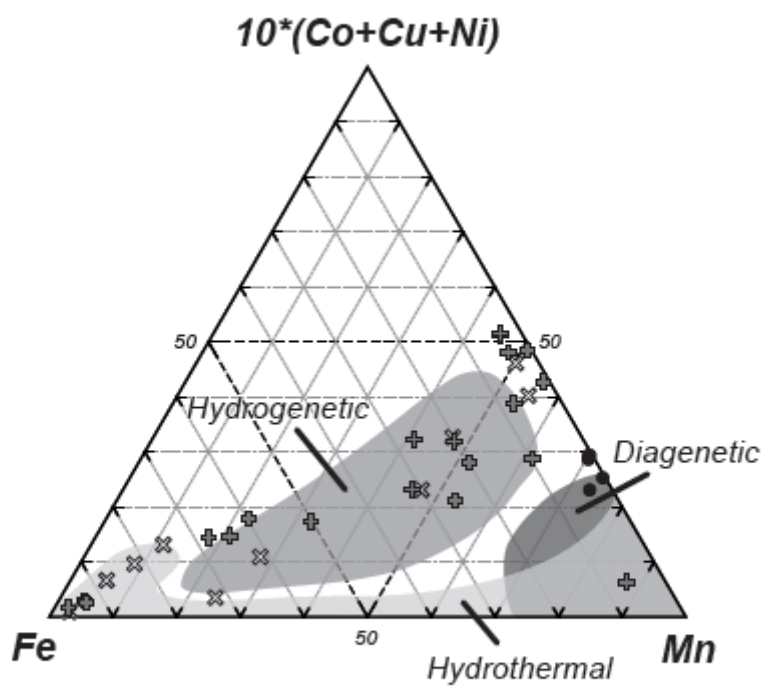


FIGURE 9

**FIGURE 10**

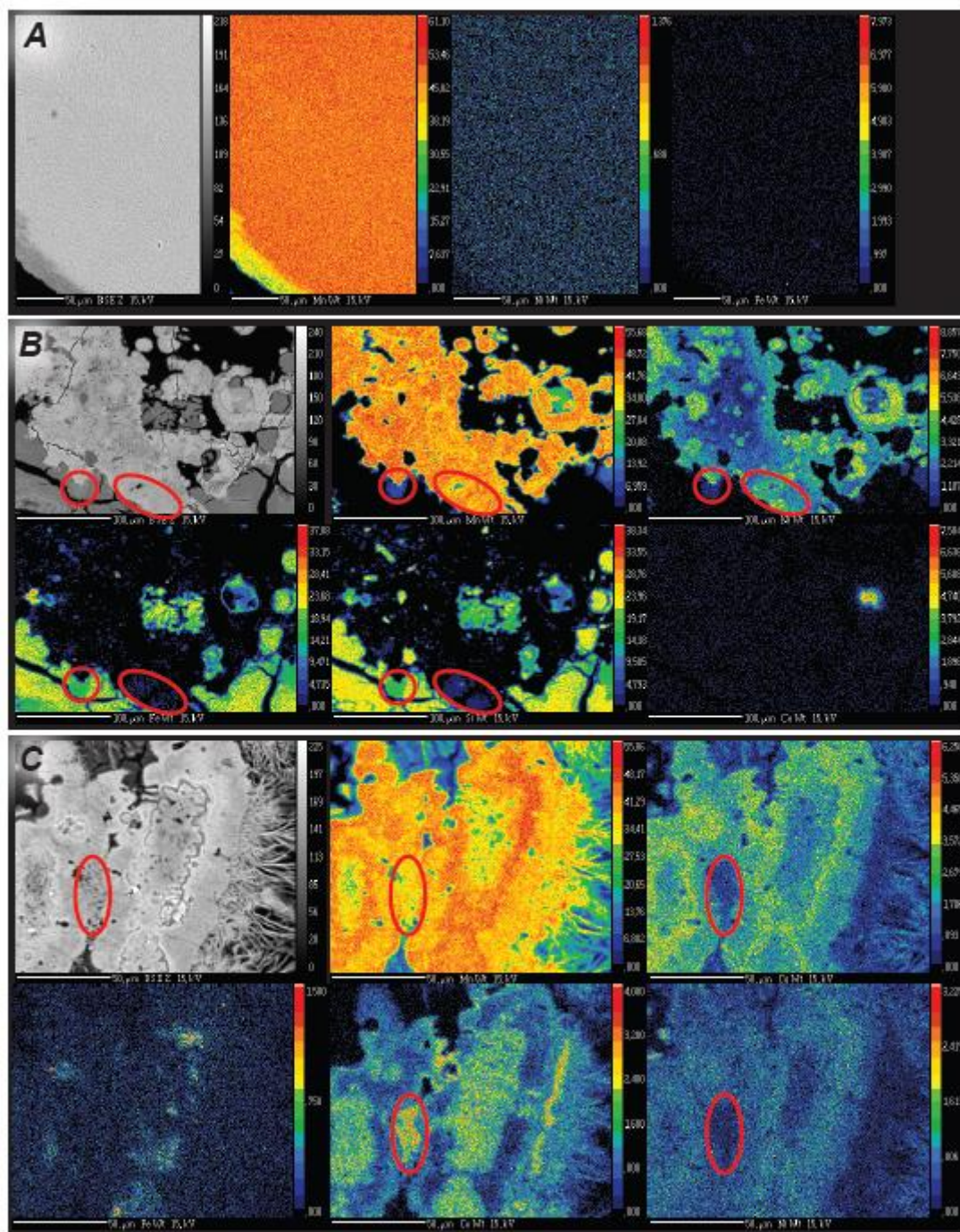


FIGURE 11

ppm		1																1																1															
V	7	7	0	6	7	2	8	7	3	7	6	2	1	5	6	0	4	9	5	5	3	3	5	3	2	2	1	7	4	3	1	3	3	4	4	4													
Co	5	5	4	4	3	4	3	8	4	2	6	1	9	3	2	2	8	2	9	6	8	0	0	4	1	9	2	9	2	8	8	6	6	6	0	4	1	4											
Ni	9	7	5	6	2	5	2	7	0	9	6	6	3	6	9	5	9	9	9	4	7	0	6	6	3	6	9	5	9	9	9	4	6	6	6	6	6												
Cu	0	4	1	4	4	6	8	1	5	0	2	1	6	4	2	4	6	1	3	3	2	1	8	5	0	7	5	1	9	2	3	6	0	3	7	5	5												
Zn	6	-	3	5	4	0	1	7	8	6	8	2	0	6	3	2	0	4	2	0	1	1	2	1	6	2	1	4	2	0	4	2	0	4	2	0	0												
As	3	1	8	1	3	2	6	4	2	8	2	4	5	1	7	3	4	9	0	0	4	2	2	6	2	1	9	3	9	7	4	0	0	0	0	0													
Rb	6	4	2	6	6	6	1	5	5	6	4	7	7	0	8	4	6	3	8	3	7	9	3	0	6	8	9	0	9	5	4	3	3	3	3	3													
Sr	0	0	3	4	8	6	6	8	9	5	6	8	9	4	9	7	2	9	0	0	2	1	2	1	2	2	2	0	4	7	3	3	1	1	1	1	1												
Y	5	7	0	3	7	2	9	6	9	2	3	9	3	3	7	4	0	6	9	8	9	1	0	5	9	3	8	3	0	4	0	4	5	5	7	7													
Zr	-	-	0	-	-	5	1	-	-	1	7	1	7	-	5	7	4	-	5	2	3	6	5	1	8	4	2	9	1	-	-	-	-	-	-	-													
Ba	4	2	3	7	0	4	1	3	1	1	5	4	6	3	2	7	9	1	5	0	0	0	4	1	5	7	0	2	2	0	8	6	6	1	5	0	7												
Mo	3	6	1	2	0	1	2	8	2	8	5	1	8	2	1	5	6	5	6	5	8	8	8	0	0	8	4	6	6	6	1	5	0	7	0	7	9	8											
V	9	7	6	9	8	1	6	9	5	7	1	6	8	8	9	0	1	8	8	6	6	7	8	9	9	0	1	8	8	6	6	6	6	6	6	6	6												
Co	7	8	9	9	0	1	8	8	9	7	1	6	8	8	7	1	6	8	8	8	6	6	7	0	6	6	1	1	1	1	1	1	1	1	1	1	1	1											
Ni	6	4	5	0	7	9	1	3	6	9	5	9	9	9	9	9	9	9	9	4	1	1	1	1	1	1	1	1	1	1	1	1	1	1	1	1	1												
Cu	9	3	1	0	5	2	4	0	5	8	2	4	0	5	2	4	0	5	8	4	7	1	4	2	1	2	1	1	2	1	1	1	1	1	1	1	1												
Zn	4	4	9	8	6	3	1	7	3	7	2	0	4	2	0	4	2	0	0	1	1	2	1	6	2	1	1	1	2	1	1	1	1	1	1	1	1	1											
As	4	2	2	6	2	1	9	3	9	7	4	9	0	0	3	9	2	5	1	8	9	2	2	2	1	8	9	2	2	2	2	2	2	2	2	2	2												
Rb	7	9	3	0	6	8	9	0	9	5	4	3	8	3	7	9	3	0	6	8	9	0	9	5	4	4	1	3	2	2	2	2	2	2	2	2	2												
Sr	7	6	5	5	8	2	0	4	7	3	1	1	2	2	4	3	1	2	2	4	3	1	2	2	2	2	2	2	2	2	2	2	2	2	2	2	2	2											
Y	9	1	0	5	9	3	8	3	0	4	0	6	9	8	1	0	2	2	2	2	2	2	2	2	2	2	2	2	2	2	2	2	2	2	2	2	2	2											
Zr	-	3	7	9	-	-	4	1	9	-	-	4	1	9	-	-	4	1	9	-	-	-	-	-	-	-	-	-	-	-	-	-	-	-	-	-	-												
Ba	6	6	1	5	0	7	0	7	9	8	6	6	1	5	0	7	0	7	9	8	1	7	4	5	1	1	3	6	6	6	1	5	0	7	0	7	9	8											
Mo	3	2	0	0	5	2	7	2	7	8	1	4	2	9	9	5	7	9	5	7	3	2	0	0	5	2	9	9	5	7	3	2	0	0	5	7	3	2											

Table 2

Sample	Site	Nature	La	Ce	Pr	Nd	Sm	Eu	Gd	Tb	Dy	Ho	Er	Yb	Lu	ΣRE E	Ce/C e*	Eu/E u*	Ce _{xs}	GR (mm.Ma ⁻¹)
FU DR 01 01	Utu Uli	Mn	10. 13	2.4 5	1.8 4	8.3 9	1.4 8	0.4 7	2.1 8	0.3 4	2.4 1	0.6 3	1.8 8	1.6 7	0.2 8	34. 2			1.6 0	
FU DR 01 03	Utu Uli	Mn	3.6 1	1.3 5	0.5 9	2.6 0	0.4 9	0.1 4	0.7 2	0.1 2	0.8 8	0.2 2	0.7 1	0.6 1	0.0 9	12. 1			1.0 8	
FU DR 01 04	Utu Uli	Fe-Si-Mn	7.7 9	4.1 1	1.2 0	5.5 0	1.0 7	0.3 1	1.6 6	0.2 7	1.9 3	0.5 0	1.5 9	1.5 0	0.2 4	27. 6			3.5 5	
FU DR 01 06	Utu Uli	Mn	13. 49	0.8 7	1.6 5	7.5 6	1.2 0	0.3 7	2.1 1	0.3 3	2.5 1	0.7 0	2.2 1	1.9 3	0.3 2	35. 2			0.1 0	
FU DR 01 07	Utu Uli	Mn	10. 84	1.9 4	1.5 5	6.9 6	1.1 3	0.3 1	1.6 1	0.2 4	1.7 3	0.4 7	1.4 6	1.1 5	0.1 9	29. 6			1.2 3	
FU DR 01 08	Utu Uli	Mn	3.5 3	3.2 5	0.7 4	3.4 0	0.7 4	0.2 7	1.1 0	0.1 7	1.1 3	0.2 8	0.8 4	0.8 0	0.1 3	16. 4			2.9 1	
FU DR 15 05	Anake le	Mn	11. 61	5.1 0	1.7 4	8.0 1	1.6 4	0.4 8	2.7 9	0.4 5	3.1 4	0.7 9	2.4 1	2.4 5	0.4 2	41. 0			4.2 9	
FU DR 15 06	Anake le	Fe-Si-Mn	32. 68	24. 26	5.7 6	25. 34	5.2 0	1.3 8	6.8 1	1.0 9	7.0 6	1.6 1	4.7 8	4.6 1	0.7 2	121 .3			21. 59	
FU DR 15 09	Anake le	Fe-Si-Mn	8.3 2	6.9 0	1.8 4	8.2 1	1.6 4	0.4 4	2.2 3	0.3 5	2.4 0	0.6 2	1.9 3	1.8 8	0.3 2	37. 1			6.0 5	
FU DR 15 10	Anake le	Mn	5.1 7	2.6 6	1.2 1	5.3 9	1.0 1	0.2 7	1.5 1	0.2 3	1.6 3	0.4 6	1.4 7	1.3 9	0.2 5	22. 7			2.1 0	
FU DR 22 02	Utu Sega	Mn	1.1 1	1.3 6	0.2 8	1.5 0	0.4 6	0.3 1	0.9 0	0.2 0	1.7 3	0.5 0	1.7 8	2.0 6	0.3 6	12. 6			1.2 3	
FU DR 22 03	Utu Sega	Mn - alt. Bas	1.5 0	5.7 2	0.5 9	3.2 4	1.1 3	0.5 5	1.7 7	0.3 5	2.5 7	0.6 2	1.9 4	1.9 8	0.3 2	22. 3			5.4 5	
FU DR 22 04	Utu Sega	Mn	1.7 3	4.6 0	0.4 7	2.5 4	0.8 2	0.5 7	1.5 3	0.3 4	2.9 4	0.8 1	2.8 5	3.1 9	0.5 5	22. 9			4.3 8	
FU DR 22 05	Utu Sega	Mn	1.6 4	1.6 3	0.4 4	2.6 4	0.9 5	0.7 9	2.0 5	0.4 7	4.0 3	1.1 1	3.5 1	3.5 6	0.6 0	23. 4			1.4 3	
FU DR	Utu	Mn	2.0	4.6	0.5	2.8	0.8	0.5	1.5	0.3	2.8	0.7	2.6	2.9	0.5	23.	1.06	1.47	4.3	2361

22 06

Sega

2 1 5 4 7 7 9 4 6 9 9 9 2 2

6

ACCEPTED MANUSCRIPT

Table 3: Selected Electron Microprobe Spot analyses of Mn oxides

Sample	Site	Nature	Mn	Fe	Si	Al	Mg	Na	K	Ca	Co	Cu	Ni	P
FU-DR01-03	Utu Uli	C	51.60	0.09	0.04	-	0.92	3.36	0.94	1.44	0.33	-	0.54	-
FU-DR01-03	Utu Uli	C	49.48	0.68	0.80	0.34	2.17	3.11	0.33	1.24	-	-	1.37	-
FU-PL08-06	Utu Uli	C	51.38	0.18	0.10	0.56	2.27	1.95	1.06	1.30	0.28	2.37	0.38	-
FU-DR15-10	Anakele	C	49.39	-	0.10	0.20	2.89	1.78	1.53	0.64	2.50	0.35	0.31	-
FU-DR15-10	Anakele	C	53.06	-	-	0.22	0.73	4.17	0.59	1.25	1.12	0.73	-	-
FU-DR15-10	Anakele	C	45.76	-	-	0.09	0.40	3.84	0.41	0.88	1.25	2.29	0.62	-
FU-DR22-03	Utu Sega	C	55.66	0.10	0.09	0.16	0.71	4.30	0.57	1.27	0.19	0.33	-	-
FU-DR22-03	Utu Sega	C	50.42	-	0.06	0.28	0.58	3.24	0.23	1.05	0.35	0.32	-	-
FU-DR22-03	Utu Sega	C	50.79	0.09	0.05	0.31	1.04	3.73	0.21	1.19	0.61	0.65	0.27	-
Mean			50.84	0.23	0.18	0.27	1.30	3.28	0.65	1.14	0.83	1.00	0.58	
Maximum			55.66	0.68	0.80	0.56	2.89	4.30	1.53	1.44	2.50	2.37	1.37	
Minimum			45.76	0.09	0.04	0.09	0.40	1.78	0.21	0.64	0.19	0.32	0.27	
SD			2.72	0.26	0.28	0.14	0.90	0.89	0.44	0.25	0.78	0.92	0.41	
FU-DR01-03	Utu Uli	MC*	52.89	0.03	0.06	-	0.47	3.93	0.31	2.13	-	-	-	-
FU-DR01-03	Utu Uli	MC*	52.88	0.10	0.07	-	0.54	3.45	0.33	2.64	-	-	-	-
FU-DR01-03	Utu Uli	MC	53.78	0.10	0.07	-	1.78	1.91	0.79	1.65	1.04	-	1.23	-
FU-DR01-03	Utu Uli	MC	49.87	0.59	0.27	0.18	0.67	3.73	0.24	1.56	-	-	4.95	-
FU-PL08-06	Utu Uli	MC	48.03	0.13	0.19	0.57	2.10	2.27	0.58	2.21	0.80	3.31	0.37	-
FU-PL08-05	Utu Uli	MC	52.36	0.34	0.06	-	1.62	3.07	0.61	1.13	0.58	-	2.18	-
FU-PL08-03	Utu Uli	MC	51.20	0.49	0.05	-	1.29	2.80	0.83	1.05	0.12	-	3.65	-
FU-DR15-10	Anakele	MC	47.37	0.32	0.14	0.31	0.84	3.89	0.72	1.21	3.54	2.80	0.29	-
FU-DR15-10	Anakele	MC	41.81	-	0.03	0.07	0.55	3.87	0.39	0.90	0.79	2.28	0.55	-
FU-DR15-10	Anakele	MC	49.40	-	-	-	0.51	3.41	1.06	0.97	2.11	0.76	0.17	-

FU-DR15-10	Anakele	MC	51.57	-	-	0.25	0.16	6.34	0.29	0.26	0.44	-	-	-
FU-DR15-10	Anakele	MC	43.80	-	-	-	0.46	2.85	0.58	1.02	1.63	0.22	0.09	-
FU-DR22-03	Utu Sega	MC	43.16	0.20	0.31	1.44	2.10	3.06	0.43	0.88	1.52	0.86	0.67	-
FU-DR22-03	Utu Sega	MC	42.73	0.09	0.30	0.72	2.07	2.34	0.21	1.38	1.21	0.95	0.17	-
FU-DR22-03	Utu Sega	MC	43.01	0.12	0.48	1.00	2.32	1.70	0.16	2.35	2.26	1.07	0.44	-
FU-DR22-03	Utu Sega	MC	46.61	-	0.17	0.98	2.26	2.88	0.22	1.10	1.45	1.10	1.16	-
FU-DR22-03	Utu Sega	MC	46.97	-	0.26	1.25	2.83	2.41	0.17	1.24	1.55	1.27	1.22	-
Mean			47.44	0.26	0.19	0.68	1.44	3.10	0.49	1.26	1.36	1.46	1.22	
Maximum			53.78	0.59	0.48	1.44	2.83	6.34	1.06	2.35	3.54	3.31	4.95	
Minimum			41.81	0.09	0.03	0.07	0.16	1.70	0.16	0.26	0.12	0.22	0.09	
SD			3.89	0.18	0.14	0.48	0.85	1.12	0.28	0.53	0.88	0.99	1.45	
FU-PL08-06	Utu Uli	AC	44.83	0.17	0.11	0.94	2.72	2.25	0.79	1.86	5.11	1.24	0.65	-
FU-PL08-06	Utu Uli	AC	42.24	0.80	2.28	2.59	2.05	2.93	0.77	2.09	1.45	1.64	0.58	-
FU-PL08-06	Utu Uli	AC	43.38	1.23	0.64	1.90	2.50	2.35	0.62	1.45	1.52	2.44	0.62	-
FU-DR15-10	Anakele	AC	46.73	-	0.15	0.20	0.47	3.19	0.48	0.69	3.97	2.09	0.91	-
FU-DR15-10	Anakele	AC	42.17	0.47	0.27	0.18	0.53	2.75	0.39	0.91	4.67	0.97	0.49	-
FU-DR15-10	Anakele	AC	48.22	0.54	0.21	0.10	0.61	3.65	0.41	0.85	3.74	2.25	0.41	-
FU-DR22-03	Utu Sega	AC	33.45	0.25	0.59	1.07	2.23	3.13	0.40	1.69	4.00	0.63	1.01	0.22
FU-DR22-03	Utu Sega	AC	34.78	0.38	0.32	1.42	3.00	2.88	0.19	4.52	5.37	1.06	0.97	0.58
FU-DR22-03	Utu Sega	AC	37.00	0.34	0.36	1.46	3.09	2.74	0.20	4.72	4.79	1.05	1.05	0.60
Mean			41.42	0.52	0.55	1.10	1.91	2.87	0.47	2.09	3.85	1.48	0.74	0.47
Maximum			48.22	1.23	2.28	2.59	3.09	3.65	0.79	4.72	5.37	2.44	1.05	0.60
Minimum			33.45	0.17	0.11	0.10	0.47	2.25	0.19	0.69	1.45	0.63	0.41	0.22
SD			5.22	0.35	0.67	0.85	1.08	0.43	0.22	1.51	1.44	0.64	0.24	0.22

Titanium was systematically below the detection limit; '-' below detection limit ; C: Crystallites; MC: Microcrystallites; AC: Amorphous cryptocrystalline oxides
 MC*: Analysis of microcrystallites of the uppermost layered and massive crust

Table 4

	Hydrothermal									Hydrogenetic Fe-Mn crusts				Pacific Fe-Mn Nodules	
	Utu Uli (n=20)	Anakele (n=10)	Dorsale Alofi (n=5)	Valu Fa Ridge (n=8)	Mariana Arc (n=26)	Tonga Arc (n=4)	Yap Arc (n=7)	Hawaii rift zone (n=11)	Galicia Bank* (n=4)	West Pacific (n=32)	West-central Pacific (n=73)	East-central Pacific (n=97)	East Pacific (n=56)	C-C Zone (n>>100)	Other Abyssal Plain (n>>100)
	This study			Hein et al (1997)					Gonzalez et al. (2016)	Hein et al (1997)				Hein et al (1997)	
Fe/Mn	0.57	1.24	0.01	0.03	0.04	0.07	0.05	0.04		1.01	0.64	0.71	1.14	0.27	0.69
%															
Si	7.00	10.07	2.00	5.10	2.30	5.10	3.20	2.20	1.45	5.80	3.00	4.60	11.40	7.60	8.80
Al	0.78	0.57	0.96	0.24	0.72	2.50	1.10	1.00	1.03	1.40	0.71	0.88	0.88	2.90	3.00
Fe	14.62	20.40	0.60	1.30	1.70	2.70	2.20	1.90	3.08	21.80	17.00	19.20	19.20	6.90	12.70
Mn	25.52	16.50	45.22	51.60	47.20	40.40	44.20	46.40	35.90	21.60	26.60	26.90	16.90	25.40	18.50
Ca	1.47	1.13	3.95	1.70	1.80	2.30	1.50	2.00	8.74	2.90	6.40	3.40	1.90	1.70	1.80
Mg	1.42	1.31	1.86	0.57	1.90	1.80	2.40	2.70	1.72	1.20	1.20	1.20	1.20	1.70	1.40
K	0.73	0.69	0.50	0.50	1.10	0.65	1.00	1.10	0.72	0.58	0.54	0.61	0.88	1.00	0.93
Na	2.81	2.35	3.21	4.30	2.70	3.40	1.90	2.80	0.77	1.90	1.90	1.90	2.00	2.80	2.10
Ti	0.10	0.05	0.09	0.03	0.51	0.15	0.09	0.23	0.11	1.10	1.10	1.30	0.60	0.53	0.78
P	0.38	0.40	0.03	0.02	0.07	0.05	0.07	0.04	1.26	0.51	1.80	0.66	0.42	0.10	0.10
ppm															
V	288	351	414	5	203	197	529	162	2073	736	725	713	626	470	480
Co	3478	2757	9675	40	96	30	450	326	10749	4427	7993	8110	3118	2400	2400
Ni	14594	3590	3050	44	330	67	4518	1585	3501	3851	5728	4926	3258	12800	6300
Cu	642	5254	4323	112	263	72	2632	83	1744	1014	1053	1187	756	10200	4200
Zn	209	274	185	95	2574	104	1621	390	429	757	870	773	694	1400	900
As	121	129	10	16	69	20	49	21	104	286	247	290	278	159	159

Sr	352	301	356	452	561	332	851	520	2161	1703	1853	1798	1397	450	700
Y	23	25	14	12	17	23	37	14	76	207	268	228	176	133	133
Ba	478	586	320	1243	1511	507	3089	883	29544	1695	2074	2033	4159	2800	2000
Mo	798	425	532	1658	663	394	324	312	184	445	562	532	382	520	360
Pb**	26	28	8	53	70	58	88	30	2484	1484	1809	1875	1373	450	820
Cd	10	13	16	0.8	20	6.1	44	28		2.7	4.1	3.5	3.2	12	11
Co + Ni + Cu (%)	1.87	1.16	1.70	0.02	0.07	0.02	0.76	0.20	1.60	0.93	1.48	1.42	0.71	2.54	1.29

Galicia Bank*: one stratabound crust (DRR41-1B) and three Co-rich hydrothermal Mn nodules (DRR81-1, DRR21-1 and DRR21-2)

Pb**: n=14 (Utu Uli), n=7 (Anakele) and n=1 (Utu Sega)

ACCEPTED MA